Journal of *Marine Science and Engineering*

MDPI

Article

Adaptive Mesh Refinement for Trailing Vortices Generated by Propellers in Interaction with Slipstream Obstacles

Jan Geese [1,*], Julian Kimmerl [1], Marc Nadler [2] and Moustafa Abdel-Maksoud [3]

[1] SCHOTTEL GmbH, Schottelstr. 1, 56281 Dörth, Germany; jkimmerl@schottel.de
[2] Faculty of Engineering, Koblenz University of Applied Sciences, 56075 Koblenz, Germany
[3] Institute for Fluid Dynamics and Ship Theory (FDS), Hamburg University of Technology (TUHH), Am Schwarzenberg-Campus 4(C), 21073 Hamburg, Germany; m.abdel-maksoud@tuhh.de
* Correspondence: jgeese@schottel.de

Abstract: The investigation of cavitating trailing vortices emerging from marine propellers is of great interest in the industry. With the help of computational fluid dynamics (CFD), studying the cavitating trailing vortices may be facilitated. However, limitations in computational power raise the necessity to execute numerical simulations as efficiently as possible. The time-efficient simulation of cavitating trailing vortices interacting with rigid bodies is especially challenging due to the continuous change of cavity locations. This study investigates the usability, capability, and practicability of automatic adaptive refinement at every calculation time step for transient Reynolds-averaged Navier–Stokes (RANS) and large eddy CFD simulations of the cavitating tip and hub vortices, utilizing the Schnerr–Sauer cavitation model, in the presence of a rudder located in the propeller slipstream and for an isolated propeller, with additional focus on the computational effort necessary for using high frequency updating adaptive mesh refinement (AMR). It is found that AMR is suitable for resolving cavities with relative motion to the propeller and in interaction with slipstream obstacles. However, the computation time is significantly increased, which renders this method useful only if a classic AMR is not possible due to geometrical limitations. Even in the cases that benefit from the automated AMR, numerical instabilities may lead to unphysical pressure fluctuations, which reduce the suitability of the method for the evaluation of underwater radiated noise.

Keywords: adaptive mesh refinement; cavitating trailing vortices; rudder interaction; underwater radiated noise; dynamic mesh

Citation: Geese, J.; Kimmerl, J.; Nadler, M.; Abdel-Maksoud, M. Adaptive Mesh Refinement for Trailing Vortices Generated by Propellers in Interaction with Slipstream Obstacles. *J. Mar. Sci. Eng.* **2023**, *11*, 2148. https://doi.org/10.3390/jmse11112148

Academic Editors: Diego Villa and Alon Gany

Received: 11 September 2023
Revised: 26 October 2023
Accepted: 7 November 2023
Published: 10 November 2023

1. Introduction

The investigation of cavitating trailing vortices originating from marine propellers is of great importance in the marine industry and academia and plays a major role in several fields of application. One example is the minimization of rudder erosion due to cavitating tip and hub vortices interacting with the rudder surfaces, as well as the design of twin propeller systems where the interaction of the tip vortex emerging from the pull propeller with the push propeller blades can significantly reduce propulsion performance. In recent years, the study of detailed vortex dynamics, especially from wing trailing vortices, is of great interest. Increased computational power allows detailed insights into this not-yet-fully understood vortex phenomenon.

Furthermore, cavitation noise, especially noise induced by cavitating trailing vortices emitted by propellers, is considered a dominant contribution to the spectrum of radiated noise [1,2]. In the frequency range from 10 to 300 Hz, an increase in the natural background noise levels in the oceans by 20 to 30 dB is measured, which is correlated to shipping operations [3] and may have a negative impact on the communication, navigation, and in the predator–prey interaction of marine mammals and fish [4]. Likewise, shipping noise interferes with sensor technology used by various human-made vessel types, and mitigation

of underwater radiated noise is a high priority due to pressure from classification societies and regulatory institutions [5]. Numerical simulations with computational fluid dynamics (CFD) are crucial in studying vortices and understanding the physical mechanisms of cavitation noise. When investigating trailing vortices of cavitating underwater propellers with CFD, it is important to model the regions where cavitation occurs with as much detail as possible. RANS and large eddy simulation (LES) approaches can resolve the cavitating trailing vortices originating from the propeller adequately if the spatial and temporal resolution is sufficiently fine in the vortex region [6,7].

Discretizing the simulation domain adequately in this area without increasing the number of cells to the extent that the computing speed is no longer justifiable in an industry environment is not a trivial task when considering the contemporary limitations in computational power. For an isolated propeller, one or more geometric shapes, such as helices or cylinders, can be manually generated to refine the area a priori through which the cavitating trailing vortex passes [8,9]. However, a study conducted by Windt and Bosschers in 2015 [8] demonstrates that using automatic AMR based on a selected refinement criterion, in this case, a jump-based estimator, can produce three times fewer grid cells at similar solution accuracy, compared to a priori refinement utilizing geometric shapes.

In 2016, Yvin and Muller [10] stated that, in the case of a tip vortex, the adaptive refinement criterion should not be a low value of the pressure since it is not certain that this region is always inside the tip vortex. Furthermore, the pressure gradient is also impractical because it is zero inside the vortex center, which would prevent refinement. Based on that, in 2021, Sezen and Atlar [11] applied a vorticity-based AMR utilizing a vortex identification criterion, namely the Q-criterion for refinement of the tip vortex emerging from an isolated propeller in combination with a rotational mesh at two stages, which resulted in an improved depiction of the tip vortex with only a small increase in computational costs. A similar method was utilized by Krasilnikov in 2019 [12], where the vorticity magnitude was chosen as the adaptive refinement criterion in combination with field functions that restrict the adaptive refinement to the tip vortex region inside a rotational mesh. In 2021, Kimmerl et al. [13,14] applied manual AMR to resolve the cavitating tip and hub vortex inside a sliding mesh to predict underwater radiated noise. For that, distance refinements were implemented with the Q-criterion, obtained from an initial converged solution. To reduce the cell count, in a second step, a distance refinement was applied, utilizing a cavitation vapor–phase interface of the cavitating tip vortex after convergence on the intermediate mesh.

Another study conducted by Kimmerl et al. in 2022 [15] demonstrates the limitations of manual AMR, where a single-step adaptive refinement is applied to resolve the cavitating tip and hub vortex of an inclined propeller. Since the rotational axis does not coincide with the inflow direction, the area of refinement for the hub vortex is conical in shape; likewise, the helix refinement for the tip vortex must be significantly increased in diameter to achieve a consistent refinement region at the expected cavity. Despite these efforts, the cavitating tip vortex is only resolved 0.75D downstream, and an additional $n = 10 \cdot 10^6$ cells are created, which increases the mesh size to an unacceptable level.

Yilmaz et al. [16,17] presented an automatic AMR approach, referred to as the Mesh Adaption and Refinement approach for Cavitation Simulation (MARCS), utilizing the commercial CFD software Star CCM+. This AMR approach uses an upper and a lower pressure threshold to resolve the cavitating tip vortex. However, other vortex identification criteria can be used [16]. In a subsequent study from Yilmaz et al. in 2019 [18], the Mesh Adaption and Refinement approach for Cavitation Simulation (MARCS) was applied to refine the cavitating tip vortex off a hull–propeller–rudder configuration with an inclined shaft. A combination of overset grid technology and a sliding mesh was applied. The overset grid covers the rudder region, which allows overlap of the tip vortex refinement and the rudder, as it is not possible to position the rudder inside the sliding mesh since it is a rigid body with no rotational symmetry with respect to the propeller rotational axis. They found that for non-uniform inflow and inclined shaft configurations, the tip vortex

cavitation disappears when the refined mesh does not match the vortex trajectory. This happens because of the relative motion between the propeller and the refined mesh regions, and they stated that re-meshing methods operating at each time step are necessary [18].

All these methods apply the adaptive refinement only at one or a few time steps, and they are accompanied by the restriction that there must be no relative motion between the propeller and the vortex refinement. This leads to special difficulties in the following cases:

- Modeling inclined propellers with non-uniform inflow;
- Existence of high gradient velocity deficits in the vessel wake;
- Simulating the flow on configurations that include obstacles in the slipstream, e.g., the rudder.

These cannot be solved with the common AMR methods for cavitating trailing vortices due to the required rotational symmetry in the numerical setup.

The limitations mentioned above give rise to the necessity for developing advanced vortex refinement methods. This study investigates the automated AMR capabilities at every time step of the CFD code HELYX version 3.5.0, which is an OpenFOAM (Open Source Field Operation and Manipulation) distribution from Engys Ltd. (London, UK). Due to the adaptivity, it should be possible to dynamically refine regions inside and outside a sliding mesh, regardless of the flow direction and additional solid boundaries. However, the extensive re-meshing increases the computational costs, which must be taken into consideration. The objective of this study is to examine whether AMR at every time step can resolve cavitating trailing vortices located in the stationary part of the mesh at any time with feasible computational effort. Additionally, it is investigated if AMR at every time step can resolve vortices and cavities in interaction with a rudder located in the propeller slipstream and what the limitations are regarding the prediction of underwater radiated noise in the form of high-frequency pressure fluctuations.

This study is structured as follows. Section 2 briefly describes the methods and fundamentals applied in this study and contains subsections about turbulence modeling (Section 2.1.1), vortex identification (Section 2.1.2), and two-phase and cavitation modeling (Section 2.2). The AMR method used in the study is described in Section 2.3. An introduction to the investigated test cases is given in Section 2.4. The computational setup necessary for functional AMR is described in more detail in Section 2.5. The results are shown and discussed in Section 3. Section 3.1 gives insight into the influence of processor imbalance due to adaptive refinement of the computational time. The adaptively refined meshes for different refinement cell sizes are investigated in Sections 3.2 and 3.3, with an analysis of the global forces for validation. Section 3.4 elaborates on the additional computational effort due to the frequent usage of AMR at every time step, followed by a demonstration of the cavitation structures predicted by using AMR. A discussion is conducted in Section 4.

2. Methods

2.1. Fundamentals Used in This Study

2.1.1. Turbulence Modeling

To capture turbulence in the CFD with feasible computational effort, modeling is necessary to approximate smaller scales. In this study, turbulence modeling is applied using two approaches. The first one uses the $k-\omega$ SST turbulence model, which is based on the RANS equations and is commonly used in the industry. It represents the flow field with ensemble-averaged velocity components [19]. Reynolds decomposition is applied, and the Navier–Stokes equation state variables are decomposed into constant Reynolds-averaged values $\overline{u}_i$, $\overline{p}$, and the transient turbulent fluctuations u_i'. The RANS equations in the incompressible form are [20]:

$$\frac{\partial(\rho\overline{u}_i)}{\partial x_i} = 0, \tag{1}$$

$$\frac{\partial(\rho\overline{u}_i)}{\partial t} + \frac{\partial}{\partial x_j}\left(\rho\overline{u}_i\overline{u}_j + \rho\overline{u_i'u_j'}\right) = -\frac{\partial\overline{p}}{\partial x_i} + \mu\frac{\partial}{\partial x_j}\left(\frac{\partial\overline{u}_i}{\partial x_j} + \frac{\partial\overline{u}_j}{\partial x_i}\right). \tag{2}$$

This results in an additional term that includes the unknown turbulent velocity fluctuations, which is referred to as the Reynolds stress term $\rho\overline{u_i'u_j'}$. The system of equations is closed following the Boussinesq hypothesis, which assumes that Reynolds stresses $\overline{u_i'u_j'}$ and the mean molecular shear stresses τ behave similarly and the extensive momentum exchange due to turbulence can be understood as an increase in viscosity [21]. Hence, an artificial eddy viscosity μ_t is introduced, which accounts for the additional momentum transfer caused by turbulent eddies. The $k-\omega$ SST model relates the Reynold stresses according to the equation [20]:

$$-\rho\overline{u_i'u_j'} = \mu_t\left(\frac{\partial u_i}{\partial x_j} + \frac{\partial u_j}{\partial x_i}\right) - \frac{2}{3}\rho k\delta_{ij}. \tag{3}$$

Eventually, the model requires two additional semi-empirical transport equations for closure. One is the transport equation for the turbulent kinetic energy k, and the second is for the specific turbulence dissipation rate $\omega = \epsilon/k$, with the turbulence dissipation rate ϵ. The second approach utilized is the LES, as it is capable of modeling the cavitating tip vortex with a significantly longer trajectory in the slipstream compared to the $k-\omega$ SST approach on the same underlying geometrical discretization, which is useful for this study. The LES is, as a result of removing time averaging and the direct calculation of large and medium scale eddies, an approach with high fidelity in depicting turbulence. Up to a certain scale, no turbulence modeling is applied. Only for small-scale motions, subgrid-scale (SGS) models are utilized. To determine a certain threshold for the resolved turbulence, the Navier–Stokes equations in incompressible form are filtered [20]

$$\frac{\partial(\rho\overline{u}_i)}{\partial x_i} = 0, \tag{4}$$

$$\frac{\partial(\rho\overline{u}_i)}{\partial t} + \frac{\partial\left(\rho\overline{u}_i\overline{u}_j\right)}{\partial x_j} = \frac{\partial\tau_{ij}^s}{\partial x_j} - \frac{\partial\overline{p}}{\partial x_i} + \frac{\partial}{\partial x_j}\left[\mu\left(\frac{\partial\overline{u}_i}{\partial x_j} + \frac{\partial\overline{u}_j}{\partial x_i}\right)\right], \tag{5}$$

where $\overline{u} = u - u'$ is the filtered velocity with a residual component u'. As a result of the filtering, the residual stress tensor $\tau_{ij}^s = -\rho\left(\overline{u_iu_j} - \overline{u}_i\overline{u}_j\right)$, solved by the subgrid-scale model, is added as an additional term in order to consider the effect of the unresolved turbulence motion on the resolved length scales. The subgrid-scale model applied in this work is the Smagorinsky model and is, similar to the $k-\omega$ SST approach, an eddy viscosity model, with the additional assumption of subgrid-scale kinetic energy being in local equilibrium and the dissipation of kinetic energy equaling production. The residual stress tensor is solved using the filtered rate of strain as follows:

$$\tau_{ij}^s - \frac{1}{3}T_{kk}^S\delta_{ij} = \mu_t\left(\frac{\partial\overline{u}_i}{\partial x_j} + \frac{\partial\overline{u}_j}{\partial x_i}\right) = 2\mu_t\overline{S}_{ij}, \tag{6}$$

where $\nu_t = \mu_t/\rho$ is the residual subgrid-scale eddy viscosity, which can be expressed as

$$\nu_t = (C_s\Delta)^2\left|\overline{S}_{ij}\right| \tag{7}$$

using the filter width Δ and the Smagorinsky coefficient C_s [20]. In HELYX and OpenFOAM, the residual subgrid-scale eddy viscosity is computed as [22]

$$\nu_t = C_k\Delta\sqrt{k_{SGS}}, \tag{8}$$

with a model constant C_k, and the subgrid-scale turbulent kinetic energy is obtained by solving

$$k_{SGS} = \left(\frac{-b + \sqrt{b^2 + 4ac}}{2a} \right)^2, \tag{9}$$

with the coefficients

$$a = \frac{C_e}{\Delta}; b = \frac{2}{3} tr(\overline{S}_{ij}); c = 2C_k \Delta (dev(\overline{S}_{ij}) : \overline{S}_{ij}), \tag{10}$$

where C_e is another model constant. In this study, the model constants are set to $C_k = 0.094$ and $C_e = 1.048$, which are the default values [22]. When utilizing the Smagorinsky model, the eddy viscosity calculated in the near wall region requires special treatment, otherwise, its value is computed too high. A Van Driest damping function can be applied to reduce the eddy viscosity in the near wall region [20].

2.1.2. *Q*-Criterion

Although the notion of a vortex is widely used in fluid dynamics and vortices are intuitively recognized, a clear, widely accepted mathematical definition for viscous flows is still missing and subject to debate. Although a vortex is often indicated by high vorticity as a good approximation, a consistent definition of vortices based only on vorticity is not possible. Many vortex identification methods are proposed. One that is well-known and commonly used is the Q-criterion, proposed in 1988 by Hunt, Wray, and Moin [23], defining a vortex as a connected fluid region with a positive second invariant of the velocity gradient tensor ∇u, with the additional condition that the pressure in the vortex region is required to be below ambient pressure. Positive values of Q represent local regions where vorticity dominates over the strain rate, indicating vortices.

2.2. Cavitation and Two-Phase Modeling

In the scope of this work, cavitation is modeled utilizing the OpenFOAM Schnerr–Sauer model [24], based on the model proposed by Schnerr and Sauer [25,26], which models the transient bubble growth and collapse process of vapor bubbles. The model considers the nuclei concentration and initial nuclei diameter necessary for the formation of the vapor bubbles. Cavitation is modeled as a two-phase flow with phase change and a dispersed volume-of-fluid approach [25,26]. The basic concept of the volume-of-fluid method is to treat the two-phase flow in distinct cells as a homogenous mixture consisting of vapor and liquid. The result is that only contiguous vapor regions with a size larger than one spatial discretization element are apparent and single bubbles are neither resolved nor transported in the domain, as illustrated in Figure 1. As the phases are collectively treated with a mixture transport equation, the shear stresses at the interface can not be considered. The two phases are considered incompressible, which reduces computational costs and is sufficiently accurate for low velocities. The mixture density for the two species ρ_m is a calculated quantity from the liquid phase fraction α and the vapor part $\alpha_v \approx 1 - \alpha$,

$$\rho_m = \rho_l \alpha + \rho_v \alpha_v. \tag{11}$$

It is noted that in the OpenFOAM Schnerr–Sauer model, the α definition in Equation (19) differs slightly from the original definition, $\alpha_v = 1 - \alpha_l$ [25,26]. Vaporization and condensation of the fluid need to be considered in the α transport equation. Thus, a source term is added on the right-hand side:

$$\frac{\partial \alpha}{\partial t} + \frac{\partial (\alpha u_i)}{\partial x_i} = \frac{\dot{m}}{\rho_l}. \tag{12}$$

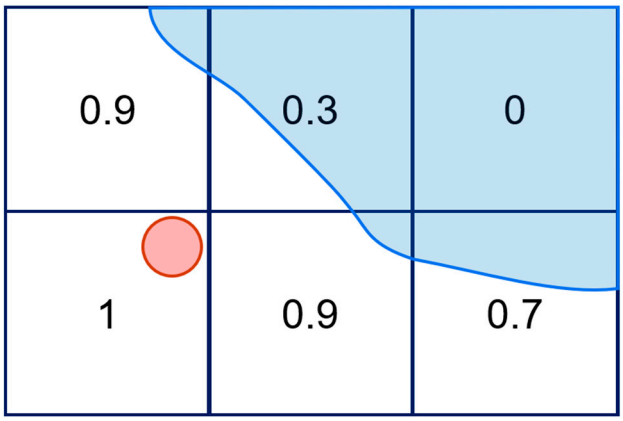

Figure 1. Illustration of volume of fluid approach. Blue: resolved vapor region; Red: unresolved single vapor bubble.

The mass transfer rate $\dot{m}$ is determined by the Schnerr–Sauer cavitation model, which is based on the Rayleigh–Plesset equation and, in turn, can be derived by physical considerations from the Navier–Stokes equations for a spherical single bubble in an infinite incompressible medium. The implementation is simplified by neglecting higher-order terms and the influence of the surface tension as well as the viscosity

$$\frac{3}{2}\left(\dot{R}\right)^2 = \frac{1}{\rho}(p_B - p). \tag{13}$$

The mass transfer rate may be calculated using the cavitation model as follows:

$$\dot{m}_\alpha^+ = C_v(1 + \alpha_{Nuc} - \alpha) \cdot p_{Coeff} \cdot \min(p - p_{sat}, p_0), \tag{14}$$

$$\dot{m}^- = C_c \cdot \alpha \cdot p_{Coeff} \cdot \max(p - p_{sat}, p_0), \tag{15}$$

with

$$p_{Coeff} = 3\rho_l\rho_v \sqrt{\frac{2}{3\rho_l}} r_{Rb}\alpha \cdot \frac{1}{\sqrt{|p - p_{sat}|} + 0.01 p_{sat}}. \tag{16}$$

Coefficients for vaporization C_v and condensation C_c are applied, and both are set to unity, which corresponds to the Schnerr–Sauer model [13]. p_{sat} refers to the vapor saturation pressure and r_{Rb} is the nucleation site radius

$$r_{Rb} = \left(\frac{4\pi n}{3} \cdot \frac{\alpha}{1 + \alpha_{Nuc} - \alpha}\right)^{-\frac{1}{3}}, \tag{17}$$

and α_{Nuc} is the nucleation volume phase fraction [25]

$$\alpha_{Nuc} = \frac{V_{Nuc}}{1 + V_{Nuc}}, \tag{18}$$

with $V_{Nuc} = \left(n\pi d_{Nuc}^3\right)/6$ from a spherical bubble. The $0.01 p_{sat}$ in the denominator of the last term of Equation (16) is a non-physical margin to avoid singularities and, thus, only a dimensionless numerical correction. While the liquid phase fraction is an explicit parameter in the model, the vapor phase fraction may be calculated. As a given volume of water V_l always contains $n = n_0 \cdot V_l$ bubbles, which may either be nuclei of radius $r_{Rb} = d_{Nuc}/2$ or vapor bubbles of arbitrary radius [25]. In the implemented model, the number of nuclei

in a discrete volume element is constant, except when the volume phase fraction reaches $\alpha = 1$, which is represented with

$$\alpha_v = \min((1 - \alpha) + \alpha_{Nuc}, 1), \tag{19}$$

and is illustrated in Table 1. The only physical parameters of the Schnerr–Sauer model that have empirical relevance are, thus, the nuclei density n_0 and the initial nuclei diameter d_{Nuc}. Although these parameters represent physical quantities, they should rather be considered as tuning parameters that influence the cavitation volume and numerical stability since they do not reflect the actual condition. In this study, the parameters are set to $n_0 = 1 \cdot 10^{12}$ m^{-3} and $d_{Nuc} = 1 \cdot 10^{-4}$ m, since it is found that these parameters yield high numerical stability combined with a detailed representation of the predicted cavities [27].

Table 1. Limiting cases of α volume phase fraction.

Case	Illustration	Explanation
$\alpha = 1 \rightarrow \alpha_v = \alpha_{Nuc}$		Only nuclei $R = R_0$ are present
$\alpha = 0.5 \rightarrow \alpha_v = 0.5 + \alpha_{Nuc}$		Nuclei $R = R_0$ and bubbles $R > R_0$ are present
$\alpha = 0 \rightarrow \alpha_v = \min(1 + \alpha_{Nuc}, 1) = 1$	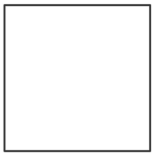	Nuclei $R = R_0$ and bubbles $R > R_0$ are present, but are reduced to fill only the volume

2.3. Adaptive Mesh Refinement

AMR automatically refines the mesh during runtime only in regions of interest. In regions that have been previously refined but no longer require a high resolution, cell refinement is removed; thus, the computational speed is increased by keeping the cell count as low as possible.

The AMR method used in this study is based on a threshold approach, where the user can choose one or more suitable flow variables, and the solver refines or coarsens hexahedral cells when a certain respective threshold is reached. This method requires relatively low computational effort and is, therefore, often used in industrial applications. However, it is not always easy to find the right threshold for refinement [28]. In general, the selection of fitting refinement criteria and thresholds is case-dependent. Usually, the refinement thresholds are defined and adjusted by hand based on an educated guess from the user. Initial simulations without an active adaptive refinement can help to identify fitting refinement thresholds. Furthermore, after running simulations with initial AMR steps, adjusting the thresholds based on the new flow field can also improve results.

For each refinement interval, the algorithm scans the selected flow field for candidate refinement cells and selects all cells that are not protected from the refinement, for example, in the case of non-hexahedral or boundary cells. Subsequently, all valid cells are split using an octree structure with a user-defined refinement level. For three-dimensional meshes, the number of cells increases by a factor of eight each time the level is increased by one. After refinement, a similar procedure is conducted for the unrefinement of cells that no longer fulfill the refinement criteria. The solution is mapped onto the newly generated

cells. Cell-centered volume fields are mapped conservatively, where newly refined child cells inherit the cell-centered value of the parent cell, and cells that undergo unrefinement receive the volume average of the cell-centered child cells. Fluxes at cell faces that possess a corresponding parent face obtain the parent's value. Fluxes at newly generated internal faces that are not generated by splitting a parent face are interpolated using the arithmetical average of the four parent faces. In order to make the flux field divergence-free, a pressure correction loop is applied [29].

When using AMR in combination with dynamic meshes, the motion function utilized prescribes the motion of the mesh only relative to the position of the cell in the last time step. The user-defined refinement level selected must be fine enough to correctly represent the desired flow phenomenon, for instance, according to literature sources, with the necessary cell size being case-dependent. However, the cell size should be set as coarse as possible to reduce computation costs.

In order to keep a smooth mesh gradient in locally refined meshes, a one-irregularity mesh constraint is implemented to limit the local difference in cell size. An irregular mesh exhibits cell vertices that are located inside of an edge of another cell, and a one-irregular mesh signifies that the irregularity of a cell in the mesh is limited to one. Cells are only coarsened if no mesh irregularity constraint prevents the unrefinement procedure. As long as the unrefinement violates the one-irregularity constraint, the affected cells remain refined.

Although AMR can dynamically adapt and refine the mesh, it is necessary to generate an initial mesh that is fine enough to depict the geometry and the physics sufficiently. In the case of a propeller simulation, a mesh independence study based on the thrust generation can help to determine the initial mesh size. The wall treatment should be defined, and the near wall region must be resolved accordingly. Additionally, it should be aimed at a complete layer coverage. Furthermore, an initial refinement should be defined in the region where AMR is expected to occur with the intention of smoothing the transition to much coarser cell levels.

2.4. Test Cases

In the following, the test cases for this study are presented. Two propellers in model scale are investigated. The first one is the "Potsdam Propeller Test Case" (PPTC) VP1304 propeller, shown in Figure 2a, manufactured at the Schiffsbau–Versuchsanstalt Potsdam GmbH (SVA) (Potsdam, Germany). Designed for validation and research purposes, the VP1304 propeller provides, depending on the operating conditions, stable tip and hub vortex cavitation along with prominent sheet and root cavitation [30]. Experimental measurements and geometric data are publicly available [31].

The second one is the E779A propeller (INSEAN, Rome, Italy) shown in Figure 2b, utilized for the examination of AMR in combination with a rudder. The geometry of the propeller and the rudder is publicly available [32]. Based on a modified Wageningen series, the propeller is highly loaded at the tip. Due to the fixed pitch and very low skew, strong tip vortices are generated. The rudder is based on an NACA0020 profile (NASA, Washington, DC, USA) and, therefore, features a symmetric geometry. The leading edge of the rudder is located $D/2$ away from the propeller plane, which coincides with the propeller generator line, and the rudder's mean line is positioned parallel to the propeller rotational axis. Over the entire rudder span of $l_s = 600$ mm, the chord length is constant with $C_R = 180$ mm. The main geometric parameters of both propellers and the investigated operation points are given in Tables 2 and 3, respectively. The rotation rate-based cavitation number is defined as:

$$\sigma_n = \frac{p_{stat} - p_v}{\frac{\rho}{2} n^2 D^2}, \tag{20}$$

where p_v refers to the saturation vapor pressure and p_{stat} to the local static domain pressure.

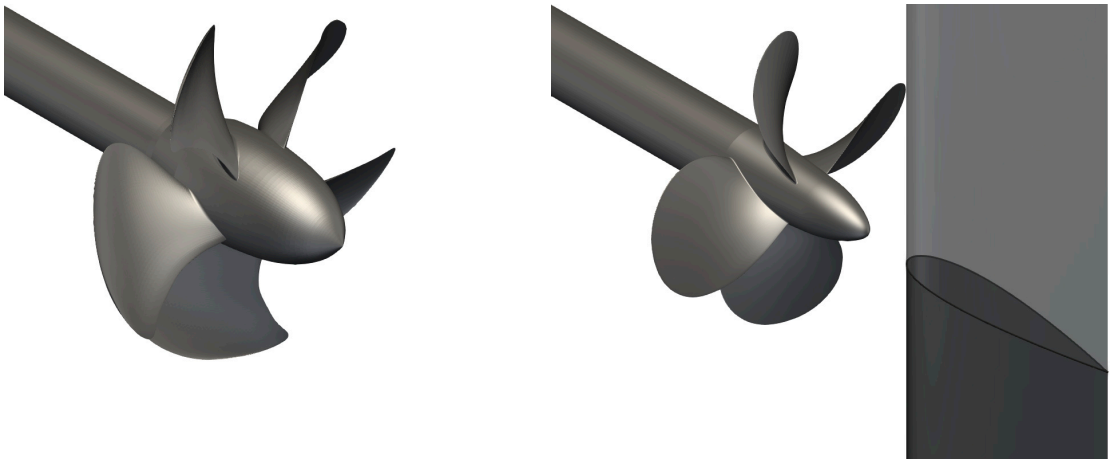

(**a**) (**b**)

Figure 2. Geometry of investigated propellers. (**a**) VP1304, (**b**) E779A with NACA0020 profile, pressure side is shown.

Table 2. Geometric data of the investigated propellers.

	VP1304	**E779A**
Diameter [mm]	250.00	227.00
Pitch ratio at 0.7R [−]	1.63	1.10
Chord at 0.7R [mm]	104.17	86.00
Area ratio [−]	0.78	0.69
Skew [°]	18.39	4.48
Number of blades [−]	5	4
Sense of rotation [−]	Right	Right

Table 3. Investigated operation conditions.

	VP1304	**E779A**
Advance ratio [−]	1.019	0.88
Rotational speed $[s^{-1}]$	24.987	25.00
Reynolds at 0.7R [−]	$1.6 \cdot 10^6$	$8.18 \cdot 10^5$
Cavitation number [−]	2.024	1.2
Domain pressure [Pa]	42,238.00	21,167.50
Domain temperature [K]	296.35	289.15
Liquid density $[kg/m^3]$	997.54	998.94
Vapor density $[kg/m^3]$	0.021	0.014
Viscosity $[m^2/s]$	$9.337 \cdot 10^{-7}$	$1.11 \cdot 10^{-6}$
K_T (wetted)[−]	0.387	–
$10K_Q$(wetted)[−]	0.976	–
K_T (cavitating)[−]	0.373	–
$10K_Q$(cavitating)[−]	0.969	–

2.5. Computational Setup

This section describes the computational setup applied for the simulations and states the main assumptions for the flow field. The finite volume method implemented in HELYX version 3.5.0 is applied to perform all numerical simulations. The solution of the

flow is obtained using the *interPhaseChangeDyMFoam* solver, capable of modeling two incompressible, isothermal, and immiscible fluids with volume of fluid interface capturing and additional dynamic mesh capabilities. The solver can model active phase change and supports the OpenFOAM Schnerr–Sauer cavitation model.

To consider asymmetric and unsteady effects in the flow field, all calculations are performed transiently and with full geometric models; no periodic behavior is assumed. Modeling of the propeller rotation is performed by applying physical rotation to a cylindrical zone of the mesh surrounding the propeller. A cyclic arbitrary mesh interface (*cyclicAMI*) boundary condition is applied to interpolate the information between the rotational and stationary parts of the mesh.

The same setup is utilized in all simulations. A pressure outlet is defined in combination with a fixed value normal surface-constrained velocity inlet. For all the propeller blades and the shaft, a rotating wall velocity boundary condition is applied. The propeller shaft is modeled without additional angular velocity as the complete cylindrical zone of the mesh surrounding the propeller is rotating. The simulations are performed under consideration of the gravity force in order to consider the hydrostatic pressure. On the wall boundaries, a fixed flux pressure condition is applied. Furthermore, all walls are modeled with no-slip conditions. The boundary layer is modeled as a high Reynolds case using the logarithmic law of the wall. Consequently, the first cell height is such that a dimensionless wall distance constraint $y^+ > 30$ is fulfilled and the first cell point fits into the log-law layer region. For both propellers, the first cell height near the propeller blade root is not sufficient to fulfill the desired $y^+ > 30$ constraint, which could lead to slight inaccuracies in the simulation. For the calculation of the turbulent kinetic energy k in the near wall region, a simple Neumann boundary condition is applied. The near wall value for ω is calculated using the OpenFOAM *omegaWallFunction*, which inherits the traits of a Dirichlet boundary condition and can switch between high and low Reynolds treatment. Based on the respective y^+ cell value, blending is performed between the viscous sublayer and logarithmic region [33]. The time is discretized such that one degree of propeller rotation is equivalent to one time step $\Delta t = 1^\circ$. In cavitating conditions and for LES, the time step is reduced to $\Delta t = 0.1^\circ$ in order to stabilize the simulation and satisfy the CFL-criterion. For all simulations, a combination of the pressure implicit with the splitting of operators (PISO) and semi-implicit method for pressure-linked equations (SIMPLE) algorithms is utilized to iterate the equation system, namely the PIMPLE algorithm. During one time step, five outer momentum predictor loops in combination with two inner pressure correction loops are utilized, which results in an initial residual of about the order of 10^{-5} at the end of the time step.

Field under-relaxation factors, listed in Table 4, are applied for the velocity u, the liquid phase fraction α, and the turbulence properties k and ω. It is found that increasing the relaxation factor with active AMR may lead to divergence. The listed values are found to achieve stable simulation conditions.

Table 4. Field relaxation factors.

Field	Relaxation Factors
Velocity $\left[\frac{\mathrm{m}}{\mathrm{s}}\right]$	0.7
Turbulent kinetic energy $\left[\frac{\mathrm{m}^2}{\mathrm{s}^2}\right]$	0.7
Specific turbulent dissipation rate $\left[\mathrm{s}^{-1}\right]$	0.5
Liquid volume fraction α $[-]$	0.95

To achieve good accuracy and stability, all gradients are calculated using a cell-limited second-order least squares scheme, except the schemes associated with α, which are calculated using central differencing. The convection-specific divergence interpolation schemes are second-order linear upwind schemes. For the convective liquid cell fraction α, a limited

van Leer divergence interpolation scheme is applied, which provides low diffusion. All other divergence interpolation schemes are central differencing-based. Time stepping is performed using a first-order implicit Euler scheme, which is considered to be inaccurate and not compatible with LES standards. However, it is found that the normally applied second-order backward scheme is prone to divergence when applying adaptive mesh refinement.

Since *interPhaseChangeDyMFoam* calculates phase change by default, it is necessary to set the saturation vapor pressure to practically negative infinity $p_v = -1 \cdot 10^{99}$ Pa to prevent cavitation inception and simulate the wetted condition. After convergence of the wetted cases, cavitation is activated by incrementally increasing p_v, as an abrupt increase in the saturation vapor pressure would lead to divergence due to numerical instabilities.

Numerical convergence of the transient solution is determined based on four properties. First, the simulation time should exceed the time that one imaginary particle needs to cross the domain in a streamwise direction. The second property is the monitoring of the initial residuals at the end of each time step, which should be in the order of 10^{-5} or less. The third property is the convergence of the global integral propeller forces and moments for a minimum of one propeller rotation. Furthermore, convergence is obtained once the Q-criterion and the α phase fraction in cavitating condition enter an angularly periodic behavior at the same phases, which is monitored using exported isosurfaces.

The flow domain of the two propellers consists of the respective cavitation tunnel test section and is visualized in Figure 3. For the VP1304 propeller, the cavitation tunnel length is $l_X = 10.3D$, with the propeller plane located at $l_{XI} = 2.8D$ away from the inlet. The propeller is centered in the $Y - Z$ plane with quadratic tunnel dimensions with a cross-section $l = 2.4D$ and rounded corners. The dimensions of the cavitation tunnel corresponding to the E779A propeller are a length of $l_X = 11.5D$, a height of $l_Y = 2.6D$, and a width of $l_Z = 2.6D$. As mentioned before, the leading edge of the rudder is located $D/2$ away from the propeller plane. Gravitational forces are applied in a negative Y direction. For both propellers, the cylindrical AMI is positioned close to the propeller to allow AMR in the stationary part of the mesh.

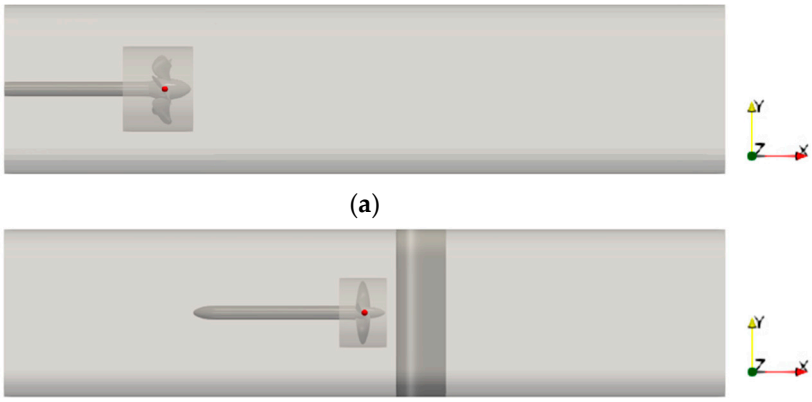

Figure 3. Numerical domain for the VP1304 propeller (**a**) and E779A propeller (**b**) with AMI, the red dot marks the origin of the coordinate system, the inlet is in the negative X-direction, the outlet is in the positive X-direction.

The initial grid size, the layer coverage, and the cell level 0 spacing for both propellers are listed in Table 5. To prevent refinement of vortical structures in regions of low interest, a protected cell zone is created in which adaptive refinement is forbidden. The outer corners of the protected zones are visualized as a dotted blue line in the detail section of Figure 4 for both propellers. This enhances the computational speed since the cell count is kept significantly lower, as, for example, the refined hub and tip vortices do not propagate too far downstream. Furthermore, the region between the tip and hub vortex is protected

since, otherwise, secondary adaptively refined vortices would lead to a strong fluctuation in the grid size and difficulties in controlling the processor imbalance, thus increasing the computational time. The protection of cells located inside the AMI is not possible since the double declaration of cell zones is forbidden.

Table 5. Main mesh characteristics for both propellers.

	VP1304	**E779A**
Mesh cell size $[-]$	$18.7 \cdot 10^6$	$30.6 \cdot 10^6$
Blade face cell size $[-]$	106,840	177,500
Rudder face cell size $[-]$	–	737,200
Layer coverage $[-]$	99.3%	99.1%
Cell level 0 spacing $\frac{\Delta s}{D}$ $[-]$	2.40	2.64

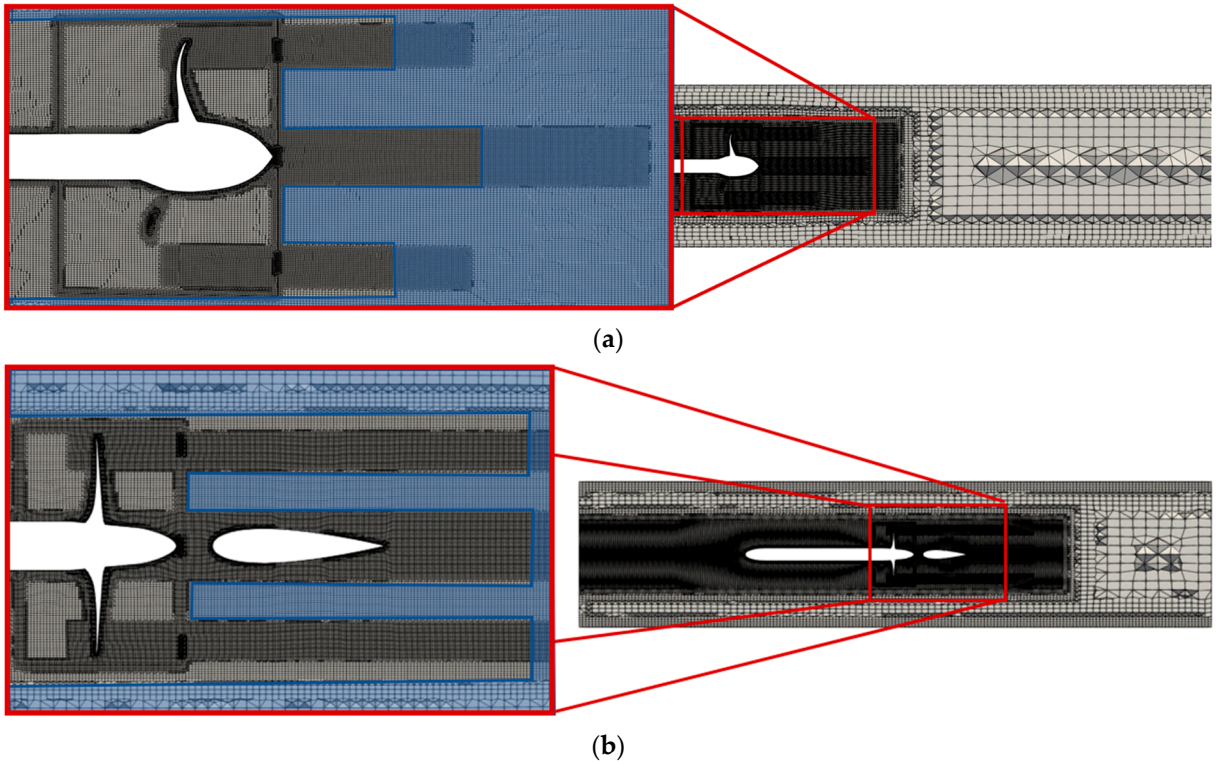

(**a**)

(**b**)

Figure 4. Initial mesh for the (**a**) VP1304 propeller and (**b**) E779A propeller with rudder. The refinement protected zone is visible in the detail section; the protected zones are shaded in blue.

To provide sufficient fine discretization in the surrounding regions of the tip vortex, an angular refinement with the length of $l_{Ref}^{Tip} = 1.25D$ for the VP1304 and $l_{Ref}^{Tip} = 2.00D$ for the E779A from the propeller plane ($X = 0.00$) is applied, with the base point at $X = -0.03$ m. This refinement furthermore smooths the transition from the adaptively refined vortex regions to the unrefined ones in the protected zone, which would otherwise lead to an abrupt increase in cell size and, thus, create numerical instabilities and inaccuracies across the refinement levels. For the same reasons, a cylindrical refinement with the length of $l_{Ref}^{Hub} = 2.00D$ is applied for both propellers. The refinements achieve a cell size of $\Delta s/D = 4.68 \cdot 10^{-3}$ for the VP1304 and $\Delta s/D = 5.15 \cdot 10^{-3}$ for the E779A.

Furthermore, it is not possible to adaptively refine boundary layer cells and the cells that determine the AMI through their faces; thus, it is necessary to apply initial distance refinements in the region of the AMI where the tip and hub vortex penetrate the interface to

ensure fine enough mesh discretization for cavitation prediction in this area. Additionally, the blade tip region is refined to allow a fine tip vortex resolution in the mixing zone. The refinements on the AMI are of cell size $\Delta s/D = 1.16 \cdot 10^{-3}$ for the VP1304 and of cell size $\Delta s/D = 1.30 \cdot 10^{-3}$ for the E779A. In the mixing zone, the mesh reaches a cell size of $\Delta s/D = 5.85 \cdot 10^{-4}$ (VP1304) and $\Delta s/D = 6.43 \cdot 10^{-4}$ (E779A), respectively. For the simulation of the E779A, distance refinements on the rudder are applied to allow cavitation to occur in the near wall region. The cell size in the mixing zone is also utilized for the adaptive refinement of the cavitating tip and hub vortex. This ensures that the grid resolution is fine enough to capture cavitation in the propeller slipstream according to experimental measurements conducted by Kuiper in 1981 [34], which determine the minimum radius of a cavitation bubble to be about $r_{cav} = 0.25$ mm. For a $D = 250$ mm model scale propeller, this corresponds to a cavitation bubble size of $r_{cav} = 1 \cdot 10^{-3} D$.

For the case of the E779A propeller with rudder, it is noted that the chosen operation point is not conducted in the experiment, as the modeled hub cap differs from the cap utilized in the experimental setups with the rudder. Nevertheless, this is not problematic since this work does not attempt to validate the AMR method's accuracy applied to the E779A propeller through experiment.

The Q-criterion is chosen as a fitting adaptive refinement parameter for resolving the tip and hub vortex. It is not easy to find a parameter threshold in which refinement should be performed. Therefore, several Q-criterion thresholds are reviewed to find the most suitable one. Based on visual observations, $Q > 20{,}000\ \mathrm{s}^{-2}$ as a threshold for the VP1304 simulation and $Q > 5000\ \mathrm{s}^{-2}$ for the E779A simulation are chosen, which generates a sufficiently large refinement for tip and hub vortex resolution. It is noted that choosing small values of about $Q < 2000\ \mathrm{s}^{-2}$ in the conducted simulations leads to strong instabilities, resulting in a cascading effect with an increasing number of cells being refined, which then results in a drastic increase in cell count and potential divergence.

When simulating cavitation, a multi-criterion refinement is applied. In addition to Q as a first refinement criterion, an additional adaptive refinement based on the α phase fraction is employed, and an $\alpha = 0.05$ lower threshold is selected. As the cell level around the α refinement is not supposed to be too coarse, the refinement based on Q acts as an intermediate step to prevent an abrupt increase in cell size.

For AMR, especially when performed at every time step in the simulation, a substantial increase in CPU time is inevitable. Processor imbalance due to AMR creates a bottleneck, which can then lead to a considerable increase in computational time. In this study, the maximum load imbalance is calculated by [29]:

$$\max\left\{\frac{nCells_i - \frac{\sum_{i=1}^{n} nCells_i}{n}}{\frac{\sum_{i=1}^{n} nCells_i}{n}}\right\},\ 1 \leq i \leq n \tag{21}$$

with the number of cells in each subdomain $nCells_i$ and the overall amount of subdomains n.

Using HELYX version 3.5.0, dynamic load balancing is not possible during simulations with an AMI. Therefore, it is necessary to perform manual load balancing in the form of processor recomposition. With this type of load balancing, the user must manually recompose the parallelized mesh after the first couple of AMR iterations, ideally when the downstream flow solution in the region of interest is already formed. Therefore, AMR should only be enabled once the initial solution is converged. It is found that the hierarchical decomposition split is best suited as it divides the domain in a structured way in all three geometric dimensions, with the aim of distributing the same number of cells on each processor. Here, the periodic behavior of the emerging vortices from the propeller blade in the slipstream is exploited, as cells constantly spin out of a processor area, which is then quickly refilled by a subsequent refinement area. This provides a relatively constant processor imbalance over time.

3. Results

3.1. Processor Imbalance

The following section evaluates the influence of processor imbalance on computational time. The influence is visualized in Figure 5.

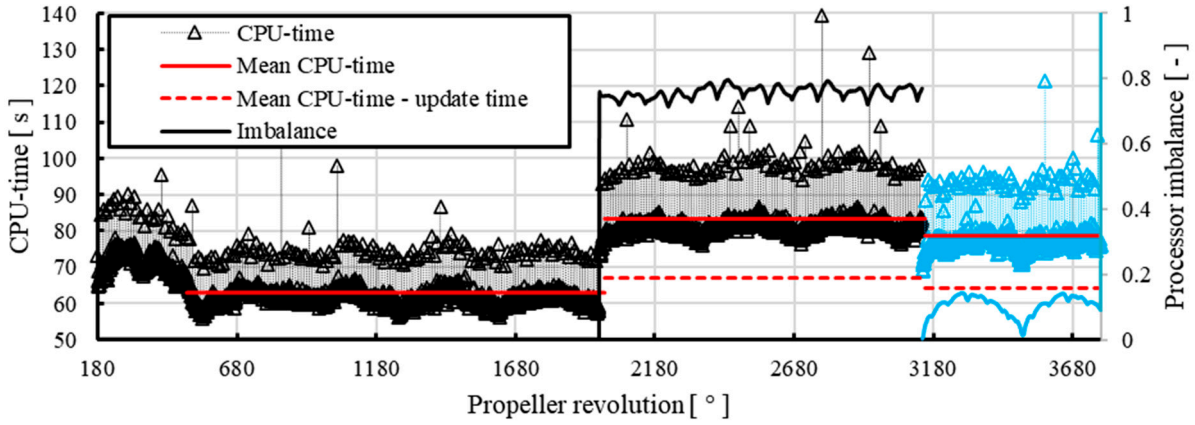

Figure 5. Processor imbalance and CPU time over simulation time, VP1304 propeller initial mesh $n_{cells} = 18.7 \cdot 10^6$, final mesh $n_{cells} = 20.2 \cdot 10^6$, CPU time after manual load balancing in blue.

The initial VP1304 mesh is refined using AMR at every time step, which results in an additional $n \approx 1{,}500{,}000$ cells. For parallelization, 160 processor cores with 2.2 GHz and 64 GB 1866 MHz DDR3 are used. At the first AMR step, an increase in CPU time, as well as an increase in processor imbalance, is clearly visible. However, besides unavoidable small fluctuations in imbalance due to varying mesh size caused by the transient flow, the value remains stable. This indicates a converged initial solution and a direct refinement of the desired region. Manual load balancing is also visible, after which a decrease in CPU time is observable. The solid red line represents the mean CPU time, with $\overline{t_{CPU}} = 63.0$ s for the initial mesh, $\overline{t_{CPU}} = 83.4$ s for adaptively refined mesh with high load imbalance, and $\overline{t_{CPU}} = 78.7$ s for the load-balanced mesh. The CPU time is reduced by $\Delta\overline{t_{CPU}} = 5.6\%$ after manual load balancing. Subtracting the significantly increased mesh updated time $\Delta t_{Mesh} = 15.3$ s for high load imbalance from $\Delta t_{Mesh} = 13.4$ s per time step for the load-balanced mesh from the overall CPU time yields the dotted red lines. It is evident that most of the increased CPU time is due to the increased mesh update time as the adaptive refinement is performed. The remaining increase in calculation time may be attributed to the imbalance and increased mesh size. For the high imbalance case, 75% of the additional CPU time is attributed to the AMR process, and for the low imbalance case, 85%. It is concluded that the processor imbalance has a significant impact on the computation speed. However, a certain level of imbalance is tolerable, as the major additional effort is associated with the adaptive refinement itself. Especially for cases with active cavitation, the processor imbalance can be a challenge, as the size of the mesh and, thus, the imbalance can fluctuate significantly due to the occasionally high fluctuations in cavity extent. Here, manual load balancing is only of limited use, as excessive manual balancing is time-consuming since it is a time-consuming task, depending on the mesh size.

3.2. Comparison of Grid Resolution

This section presents the results of the adaptively refined meshes for both propellers. First, the results for the VP1304 propeller, calculated with RANS, are shown in Figure 6. Two different refinement cell sizes are applied in wetted conditions. When comparing the grids, it is evident that AMR works well with the chosen criteria. A well-targeted refinement of the tip and hub vortex region, inside and outside of the AMI, in combination with a stable solution, is achieved. However, the finer refinement level in wetted conditions increases the solution accuracy by refining secondary trailing edge vortices up to the blade

tip, which is observed to a lesser extent for the coarser level, as visualized in Figure 7, where secondary trailing edge vortices only emerge near the root. Looking at the stationary part of the mesh, one can see that the adaptive refinement is only performed before the solution of the next time step and, therefore, does not refine the new, not yet refined cells that fall within the refinement thresholds at the current time step. This is indicated by the isosurface of the Q-criterion, which corresponds to the value of the lower refinement limit and, thus, indicates cells to be refined, being coarser at the position to which the rotating tip vortex newly moved within the current time step, showing that these cells are not yet refined but fall within the valid refinement threshold. On the other hand, the part of the mesh that the tip vortex trajectory enters at the current time step is not refined yet. This issue is significantly pronounced for the finer refinement level, as the refinement cell size is smaller at a constant time step. Furthermore, this behavior can lead to numerical instabilities in the flow field and, consequently, to unphysical Q-criterion, and, thus, refinement cascades within the domain. When using the PIMPLE algorithm, a solution could be to perform AMR at every outer corrector loop; in this way, the newly calculated flow field can be detected by the AMR algorithm, and the stability should be enhanced. However, this would increase the simulation time significantly, probably to an unfeasible level.

An interesting observation in the cavitating condition is the interaction between the cavitating tip vortex and the Q-criterion, as the latter takes the shape of the enclosed cavity, also visualized in Figure 7d.

The results of AMR with RANS in combination with the E779A with rudder are presented in the following. Similar to the VP1304 propeller, three different cases with various refinement cell sizes are simulated: two in wetted conditions utilizing a coarse and a fine refinement cell size and one in a cavitating condition. However, the cavitating tip vortex is not propagating far downstream in this case. Thus, only the two wetted cases are visualized in Figure 8 and compared with the initial mesh.

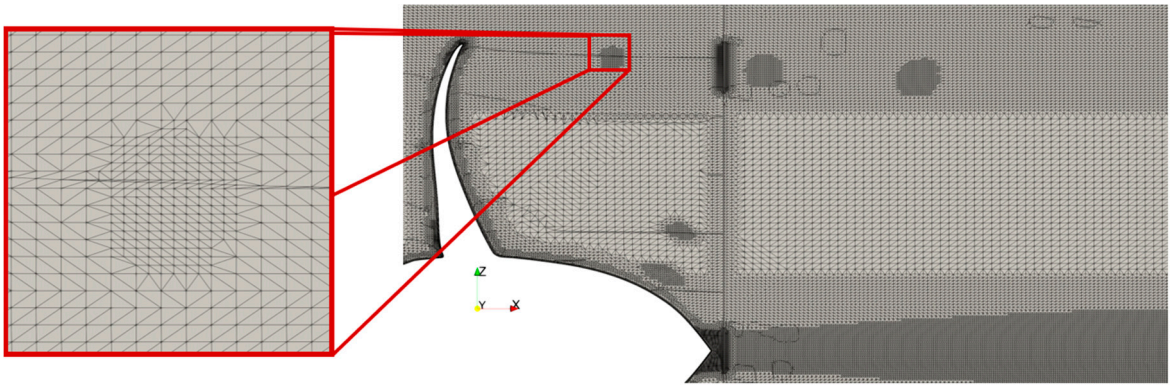

(**a**)

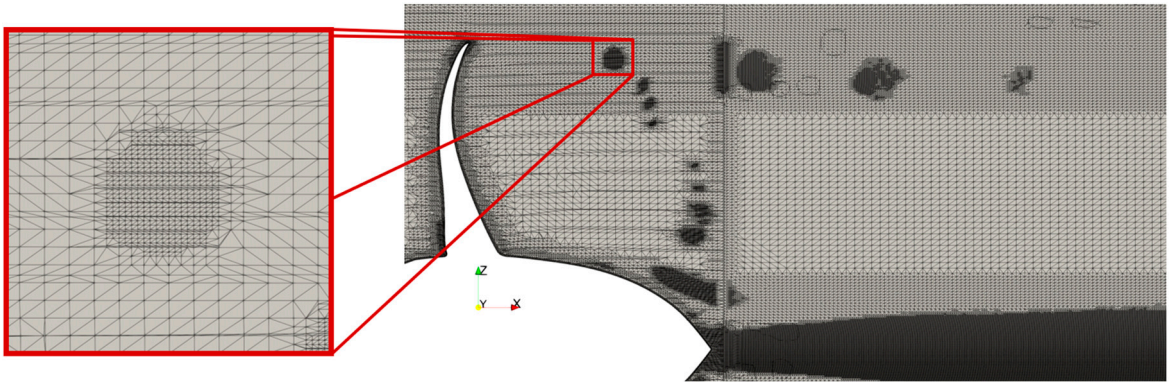

(**b**)

Figure 6. *Cont.*

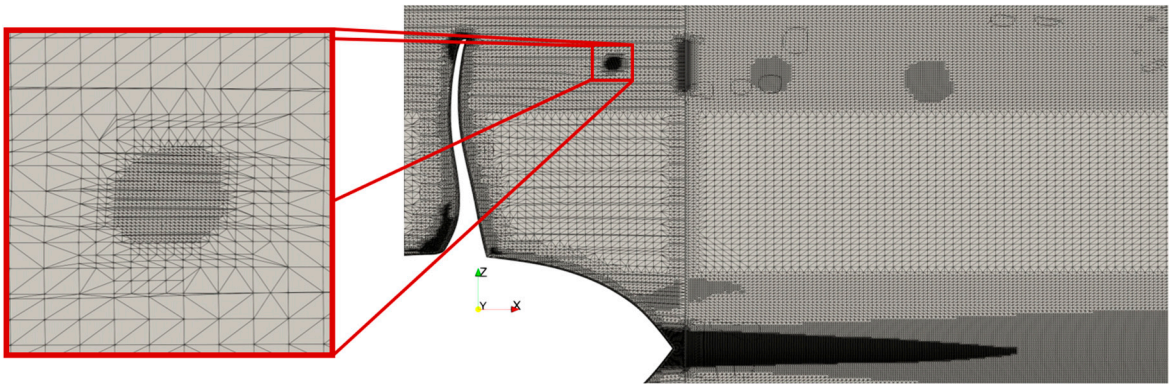

(**c**)

Figure 6. Results of AMR for the VP1304 propeller using the $k-\omega$ SSTturbulence model, (**a**) wetted condition, coarse AMR, AMR criterion: $Q > 20{,}000\ \mathrm{s}^{-2}$, refinement cell size $\frac{\Delta s}{D} = 2.36 \cdot 10^{-3}$, $n_{cells} = 20.2 \cdot 10^{6}$. (**b**) wetted condition, fine AMR, AMR criterion: $Q > 20{,}000\ \mathrm{s}^{-2}$, refinement cell size $\frac{\Delta s}{D} = 1.16 \cdot 10^{-3}$, $n_{cells} = 29.6 \cdot 10^{6}$. (**c**) cavitating condition, AMR. 1. AMR criterion $Q > 20{,}000\ \mathrm{s}^{-2}$, refinement cell size $\frac{\Delta s}{D} = 2.34 \cdot 10^{-3}$, 2. AMR criterion: $\alpha > 0.05$ refinement cell size $\frac{\Delta s}{D} = 5.85 \cdot 10^{-4}$, $n_{cells} = 34.7 \cdot 10^{6}$.

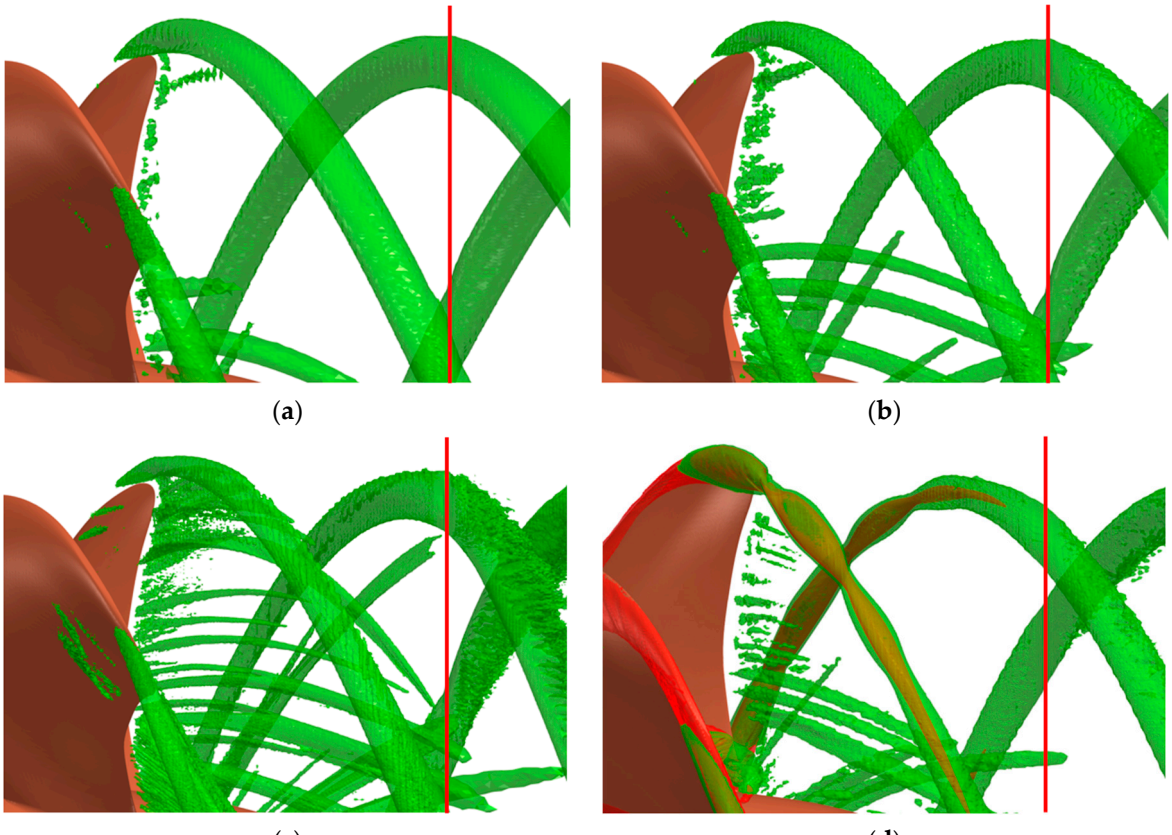

(**a**) (**b**)

(**c**) (**d**)

Figure 7. Detailed view of $Q = 20{,}000\ \mathrm{s}^{-2}$ isosurfaces for (**a**) wetted condition, initial mesh, (**b**) wetted condition, coarse AMR, (**c**) wetted condition, fine AMR, (**d**) cavitating condition, AMR, $\alpha = 0.5$ isosurfaces in red, solid red lines marks the position of the AMI, VP1304 propeller.

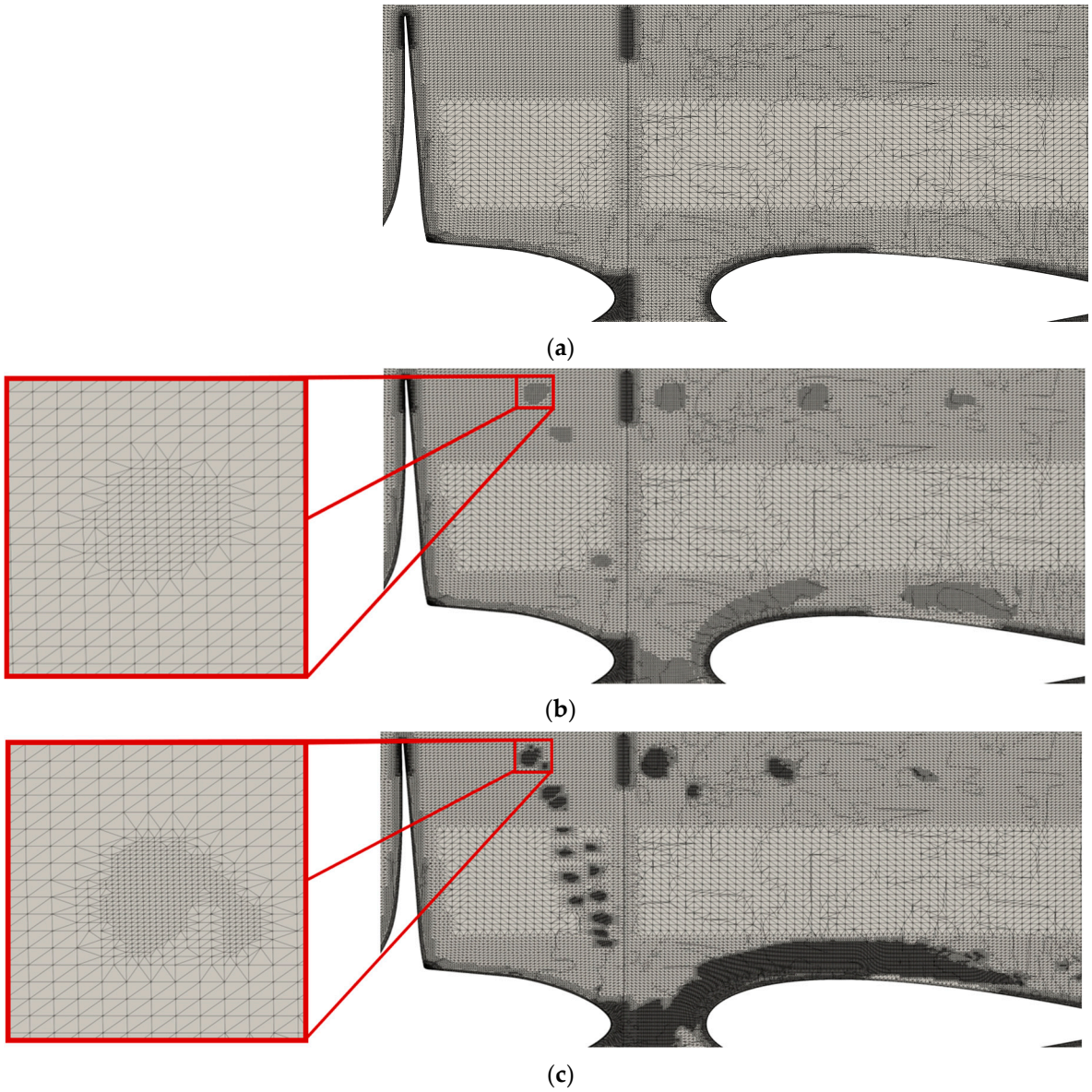

Figure 8. Results of AMR for the E779A propeller with rudder using the $k-\omega$ SST turbulence model, (**a**) wetted condition, initial mesh, No AMR, $n_{cells} = 30.6 \cdot 10^6$. (**b**) wetted condition, coarse AMR, AMR criteria: $Q > 5000\ \mathrm{s}^{-2}$, refinement cell size $\frac{\Delta s}{D} = 2.58 \cdot 10^{-3}$, $n_{cells} = 31.6 \cdot 10^6$. (**c**) wetted condition, fine AMR. 1. AMR criteria $Q > 5000\ \mathrm{s}^{-2}$, refinement cell size $\frac{\Delta s}{D} = 1.30 \cdot 10^{-3}$; $n_{cells} = 34.2 \cdot 10^6$.

It is evident that a targeted refinement of the tip and hub vortex is achieved. Additionally, with the help of the a priori distance refinement at the rudder leading and trailing edge, a seamless transition between the adaptively refined region and the protected boundary layer is possible, which is necessary to model the interaction between the vortex and rudder.

As for the VP1304 propeller, the same observations are made with regard to the increasing amount of emerging secondary trailing edge vortices for finer refinement cell size, visible in Figure 9. Moreover, with finer refinement cell size, the calculation of the tip vortex for the current time step in a coarser mesh, due to the adaptive refinement only executed at the beginning of the PIMPLE loop, is clearly identifiable in the stationary part of the mesh. Furthermore, for the finer refinement cell size, high values of Q emerge behind the rudder, which could be associated with an improved resolution in the shear layer, visible in Figure 10. However, at this refinement cell size, high Q values are also occurring

all along the propeller shaft, partly visible and marked with a blue rectangle in the figure, which are considered unphysical since they originate upstream of the propeller. Thus, it is assumed that the additional Q in the shear layer is also due to numerical instabilities rather than finer flow resolution.

Additionally, it is observed that with higher cell refinement, the Q-isosurface extends less in the downstream direction. This could be due to higher dissipation in the flow, as it is evident that the finer refinement cell size but the same downstream propagation extent of the tip vortex leads to coarser discretization results. This can be attributed to the adaptive refinement limited only to the first iteration of the PIMPLE loop. This phenomenon is also observed in the VP1304 simulations.

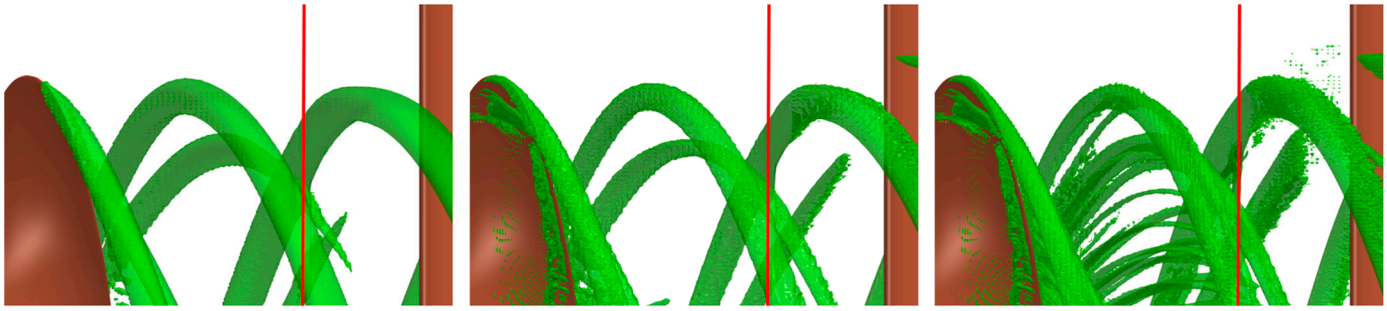

(**a**) (**b**) (**c**)

Figure 9. Detailed view of $Q = 5000\ s^{-2}$ isosurfaces for (**a**) wetted condition, initial mesh, (**b**) wetted condition, coarser AMR, (**c**) wetted condition, finer AMR, solid red lines mark the position of the AMI, E779A propeller with rudder.

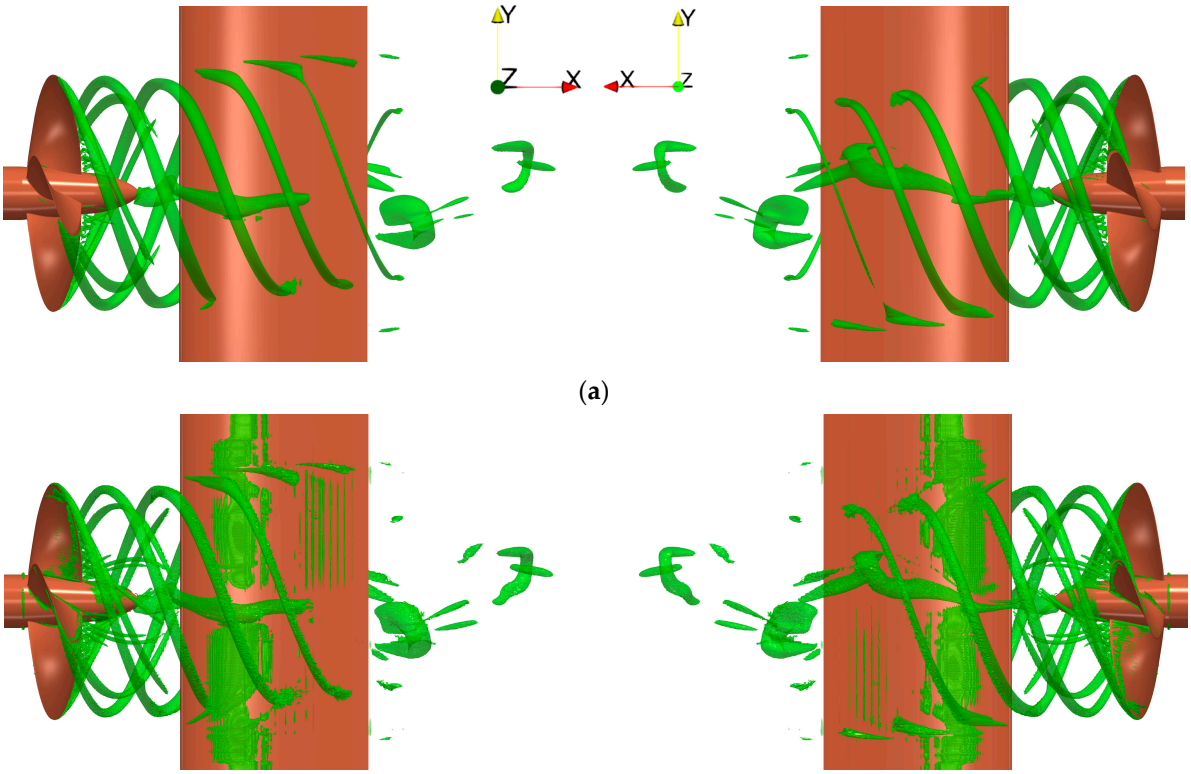

(**a**)

(**b**)

Figure 10. *Cont.*

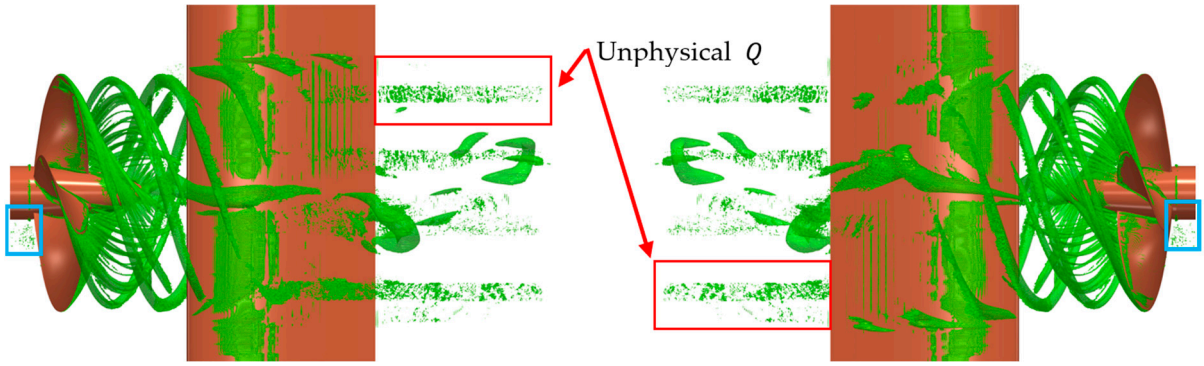

(**c**)

Figure 10. Side view of $Q = 5000\ \mathrm{s}^{-2}$ isosurfaces for (**a**) wetted condition, initial mesh, No AMR, $n_{cells} = 30.6 \cdot 10^6$. (**b**) wetted condition, coarse AMR, AMR criteria: $Q > 5000\ \mathrm{s}^{-2}$, refinement cell size $\frac{\Delta s}{D} = 2.58 \cdot 10^{-3}$. (**c**) wetted condition, fine AMR, E779A propeller with rudder. 1. AMR criteria $Q > 5000\ \mathrm{s}^{-2}$, refinement cell size $\frac{\Delta s}{D} = 1.30 \cdot 10^{-3}$.

It should be mentioned that in Figures 9b,c and 10b,c, the additional Q-isosurface near the propeller and rudder wall, not present on the initial mesh screenshot in Figures 9a and 10a, is only due to a lower wall distance specified for the isosurface sampling of Q, as all values below a certain wall distance are excluded from sampling the isosurface for clarity.

3.3. Global Forces

The integral forces obtained from the CFD are presented in the following. For the VP1304 propeller, the dimensionless thrust coefficient K_T for different adaptive refinement cell sizes, predicted by the $k-\omega$ SST model in wetted conditions, is presented in Figure 11 and compared with the experimentally measured thrust [31]. It is clearly visible that the solution on the initial mesh and with the coarser refinement cell size is converged regarding the thrust development. Compared to each other, the solutions show no difference in the predicted average integral thrust and torque. Compared to the experimental measurements, only a small deviation of $\Delta K_T = -2.4\%$ in thrust and of $\Delta K_Q = 0.4\%$ in torque is observed. However, for the finer refinement cell size, a shift in thrust and torque is observed. The difference to the experiment in thrust increases to $\Delta K_T = -2.9\%$ and in torque reduces to $\Delta K_Q = -0.02\%$. Overall, the factors causing the shift in the predicted thrust and torque that occurs for the finer refinement cell size are not clearly resolved. The reasons could be the numerical instabilities occurring during the simulation with the finer cell level, which result in pressure peaks occurring in the domain at cells that are coarsened during the AMR steps. These instabilities are the reason for the local peak of the blue line, visible in Figure 11.

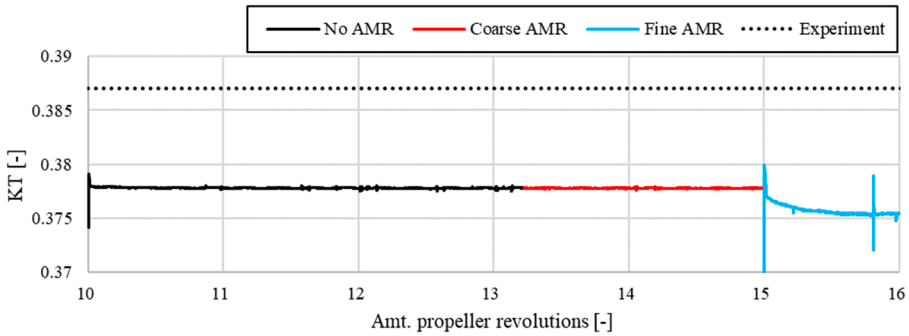

Figure 11. Predicted thrust coefficient K_T for different refinement cell sizes, RANS, wetted condition, VP1304.

In cavitating conditions, this phenomenon is significantly amplified. Strong fluctuations in thrust and torque for the adaptively refined mesh occur, as shown in Figure 12. The unphysical pressure pulses, visualized and marked in red in Figure 13c, could be associated with mapping issues during the refinement, which creates unphysical fluxes and discontinuous gradients. Compared to the experimental measurement, on average, these values do not deviate strongly. However, the unphysical pressure peaks occurring in the domain are highly problematic for the numerical prediction of underwater radiated noise. It is necessary to overcome this problem, as one of the underlying goals of this work is the utilization of AMR in combination with numerical prediction of underwater radiated noise. Obviously, these pressure fluctuations influence the sound pressure calculated by the numerical solution.

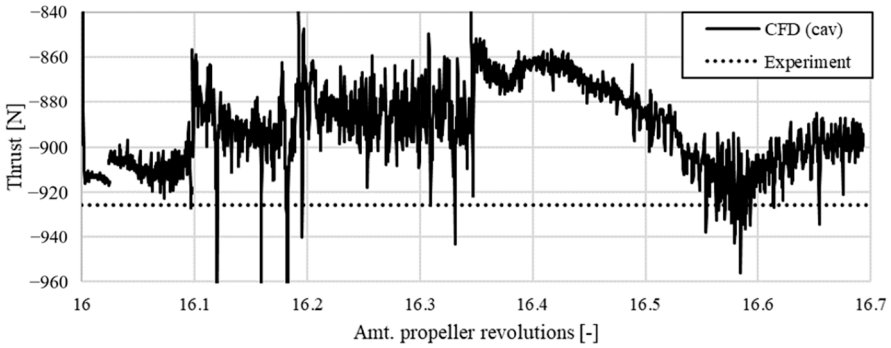

Figure 12. Predicted thrust coefficient K_T in cavitating condition, RANS, VP1304 propeller.

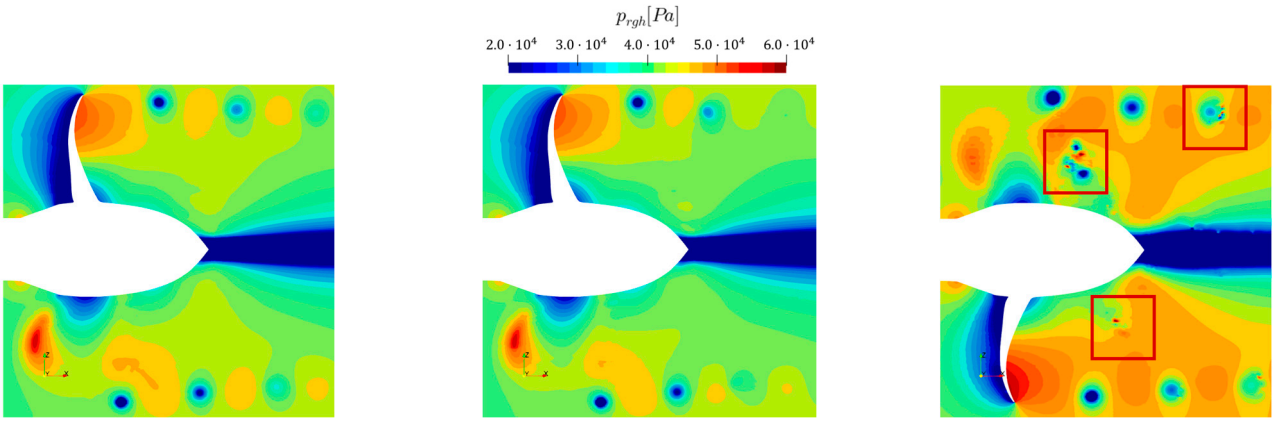

(**a**) (**b**) (**c**)

Figure 13. Domain pressure midplane for (**a**) wetted condition, coarser AMR, (**b**) wetted condition, finer AMR, (**c**) cavitating condition AMR, VP1304 propeller.

As shown above, this issue is strongly reduced when simulating without active phase change in combination with AMR, without changing any other parameter or numerical scheme. Several tests with different interpolation schemes, a maximum CFL value below one, and LES are conducted. However, the influence of the variation of the interpolation schemes on the observed problem is negligible.

For the E779A simulation, no experimental measurements are available for comparison. Thus, only a comparison of dimensionless thrust and torque on the propeller for the different AMR refinement cell sizes is visualized in Figure 14. Similar to the VP1304, a shift in value is observed for the finer refinement cell size. The upstream influence of the rudder on the predicted thrust and torque is observed, as the values exhibit a periodic behavior in blade passing frequency with four peaks in thrust occurring during one propeller revolution.

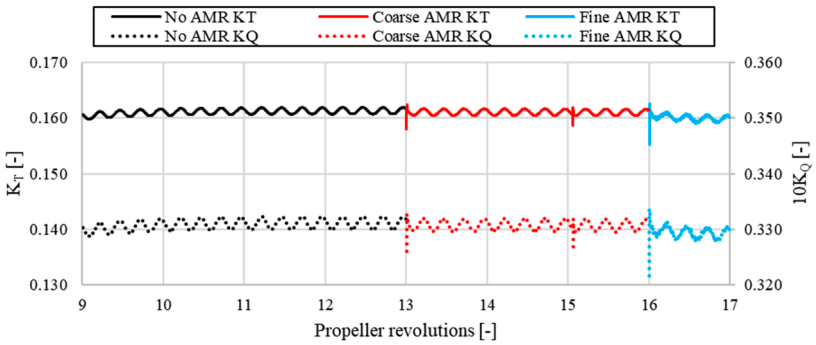

Figure 14. Predicted thrust coefficient K_T and torque coefficient K_Q for different refinement cell sizes, RANS, wetted condition, E779A with rudder.

3.4. Comparison of Computational Efforts

In the following, the computation time with and without AMR is evaluated. For the VP1304 propeller, Table 6 presents the grid sizes, average imbalance, and CPU time for the different refinement levels. Additionally, results for the LES with the Smagorinsky SGS model are presented. Furthermore, a comparison is made with a one-time adaptively refined tip and hub vortex implicit LES from Kimmerl et al. in 2021 [13], for which similar processor cores are used. All simulation efforts are scaled to $n = 100$ processor cores under the assumption of a linear relationship between CPU time and processor count. Obviously, the simulation time increases with increasing mesh size and processor imbalance. The growing average imbalance indicates that the mesh size increasingly fluctuates with finer numerical discretization. Especially for the cavitating cases, strong variations in mesh size are present as the behavior of the cavitation is highly transient, as visualized in Figure 15. Thus, it is not possible to achieve a constantly small processor imbalance, as manual reconstruction is too time-consuming when performed too often. The implicit LES [13] calculation is performed with two different time steps, which results in different CFL numbers. To obtain a stable solution for the implicit LES, one must fulfill the mean $CFL < 1$ condition, which is a requirement for LES. However, it is noted that the LES Smagorinsky SGS simulation is stable with a maximum $CFL \approx 10$, and thus, no smaller time stepping is performed. When comparing the adaptively refined cavitating RANS simulation with one-time adaptive refined ILES calculation, an increase in time by a factor of three is evident, which demonstrates the substantial increase in CPU time when performing adaptive refinement at every time step.

Table 6. Numerical metrics of AMR for the VP1304 propeller.

	Average Mesh Size [-]	Average Imbalance [-]	Average $\frac{CPU-time}{\Delta t}$ [s]	Effort $\frac{revolution}{100 \cdot CPUs}$ [d]	PIMPLE Loop [-]
RANS no AMR	$18.7 \cdot 10^6$	0.01	63.01	0.42	Inner: 2 Outer: 5
RANS coarser AMR	$20.2 \cdot 10^6$	0.11	78.71	0.53	Inner: 2 Outer: 5
RANS finer AMR	$29.6 \cdot 10^6$	0.31	111.16	0.73	Inner: 2 Outer: 5
RANS AMR (cav)	$34.7 \cdot 10^6$	0.80	101.15	6.70	Inner: 3 Outer: 3
LES AMR (cav)	$46.0 \cdot 10^6$	0.95	129.60	8.6	Inner: 3 Outer: 3
ILES a priori AMR (cav) $CFL \approx 7$ [13]	$35.5 \cdot 10^6$	–	36.00	1.50	Inner: 3 Outer: 2
ILES a priori AMR (cav) $CFL < 1$ [13]	$35.5 \cdot 10^6$	–	33.60	14.00	Inner: 1 Outer: 1

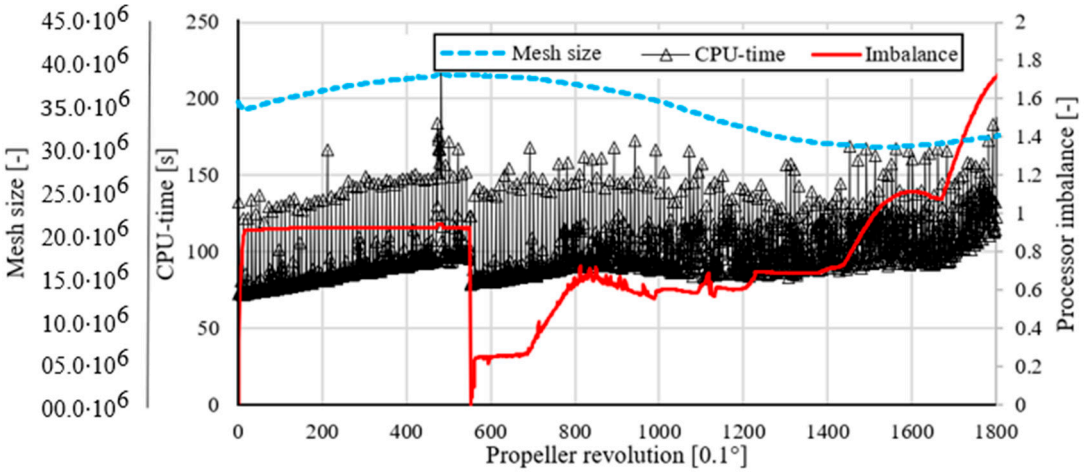

Figure 15. CPU time, mesh size, and processor imbalance for a half propeller revolution in cavitating conditions with RANS, VP1304 propeller.

For the E779A with rudder, the average computational efforts for the different adaptive refinement cell sizes for RANS and LES are compared with the initial mesh in Table 7. It is worth mentioning that after manual load balancing is performed, the processor imbalance is much more constant and at an overall lower imbalance for the coarser refinement cell level compared to simulations with the VP1304 propeller. It is not clear what causes this effect; however, it is assumed that the rudder as a second solid object with a high cell count evens the processor imbalance in the domain. Furthermore, the lower number of propeller blades, i.e., four compared to five, could influence the balance as it favors hierarchical decomposition in cartesian coordinates. Manual load balancing is performed once after a new refinement cell size is applied. The simulation with the finer refinement cell size exhibits a high CPU time because no load balancing is performed after increasing the cell level; thus, these are not representative values.

Table 7. Results of AMR for the E779A with rudder.

	Average Mesh Size [-]	Average Imbalance [-]	Average $\frac{CPU-time}{\Delta t}$ [s]	Effort $\frac{revolution}{100 \cdot CPUs}$ [d]	PIMPLE Loop [-]
RANS no AMR	$30.6 \cdot 10^6$	0.0035	60.30	0.50	Inner: 2 Outer: 5
RANS coarser AMR	$31.6 \cdot 10^6$	0.072	82.70	0.66	Inner: 2 Outer: 5
RANS finer AMR	$42.5 \cdot 10^6$	3.37	352.33	2.84	Inner: 2 Outer: 5
RANS AMR (cav)	$34.2 \cdot 10^6$	0.31	81.80	5.20	Inner: 3 Outer: 3
LES AMR (cav)	$36.5 \cdot 10^6$	0.73	111.44	7.50	Inner: 3 Outer: 3

The huge increase in computational effort for the simulations with active phase change is mostly associated with the finer temporal resolution as the time step is reduced from $\Delta t = 1°$ to $\Delta t = 0.1°$, which is necessary to avoid divergence of the calculations.

3.5. Cavitation Structures

In Figure 16, the predicted cavities for the VP1304 propeller utilizing the RANS $k-\omega$ SST and the LES Smagorinsky SGS model with time step-activated AMR are compared with snapshots from high-speed videos taken during the experiment. The gaseous fraction is visualized with $\alpha = 0.5$ isosurfaces. Overall, good agreement with the experiment is

achieved. As found in other numerical studies of the VP1304, the sheet cavitation at the propeller's leading edge is overpredicted, for which the LES exhibits slightly less chordwise extent in comparison. The root cavitation on the blade is predicted well, regardless of the model. Nevertheless, the LES exhibits less cavity volume near the root, which is closer to the experiment. Additionally, detailed small-scale cavitation structures propagating in the propeller slipstream are observed for the LES, which is also found in the experiment. This is worth mentioning, as it is not observed in previous studies of the VP1304, and thus, it is associated with the adaptive refinement, demonstrating that runtime AMR can increase the level of detail for the cavitation simulation. It is apparent that the cavitating tip and hub vortex propagate further downstream into the propeller slipstream when using LES. Further propagation of the cavitating trailing vortices is prevented by the refinement-protected cell zone. In general, the more sophisticated modeling approach without time-averaging and with the direct resolution of many of the turbulent length scales is clearly identifiable by the higher level of detail.

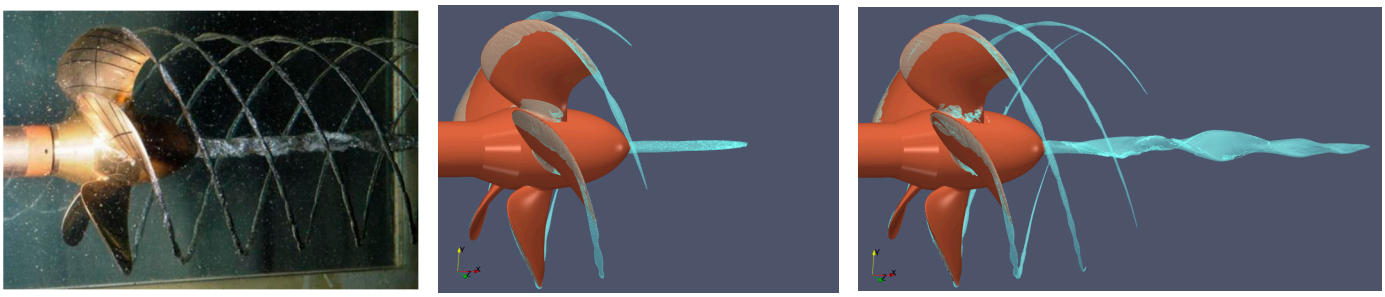

(**a**) (**b**) (**c**)

Figure 16. Comparison between experiment and cavitation α isosurfaces, (**a**) experimental observation [31], (**b**) RANS, (**c**) LES, VP1304 propeller, $\sigma_n = 2.024$.

The cavitating tip and hub vortex are also captured outside the AMI and inside the stationary part of the mesh, which shows that the AMI does not prevent the propagation of the cavity further downstream due to numerical reasons, such as interpolation issues on the AMI interface, which would render the application of runtime AMR useless.

A direct comparison between the a priori refined implicit LES from Kimmerl et al. in 2021 [13] and the explicit LES with the Smagorinsky SGS model and runtime AMR is visualized in Figure 17. While similar results are obtained, the major difference is that the cavitating hub vortex experiences more spirality in shape for the adaptively refined solution. Overall, the extent of the cavitating tip and hub vortex is comparable with the one-time refinement method, and the amount of information is maintained. Furthermore, the results are compared with the AMR study from Krasilnikov in 2019 [12]. In this study, AMR is performed only at one time step, utilizing improved delayed detached eddy simulation (IDDES) with a refinement criterion based on the vorticity magnitude. The results obtained in this study are in satisfactory accordance, with the main difference observed in the trailing vortices' extent. This is due to the fact that a refinement-protected cell zone is defined in this study, which limits further propagation of the tip and hub vortices. Overall, the comparisons prove that runtime AMR is a viable solution for refining and modeling propeller-induced cavitation in the slipstream.

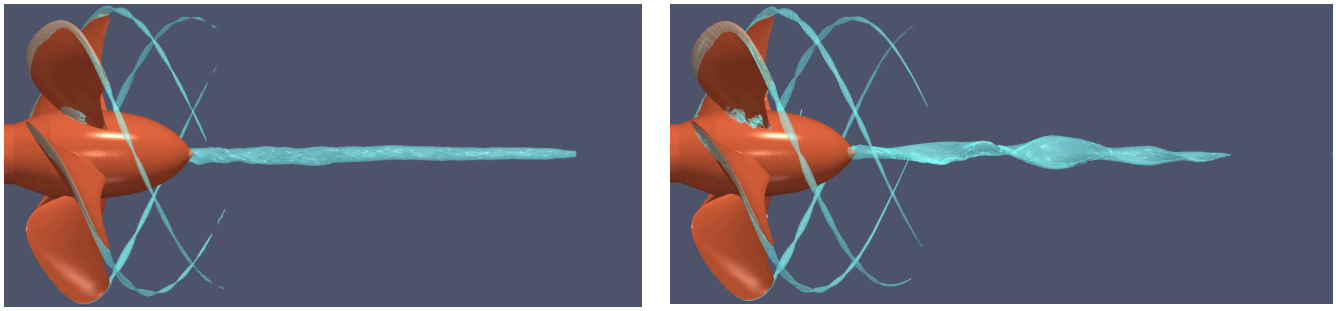

(**a**) (**b**)

Figure 17. Comparison between (**a**) a priori refined implicit LES [13] and (**b**) LES with AMR, VP1304 propeller.

For the investigated E779A propeller with the rudder configuration, the predicted cavities are shown in Figure 18. It is apparent that the cavitating tip vortex is not propagated far into the propeller slipstream. When using the high-fidelity LES approach, the tip vortex extends slightly further. It is assumed that the propagation of the cavitating tip vortex is prevented due to a periodical termination of the cavity after passing the twelve o'clock position of the propeller due to the stagnation pressure induced by the rudder, as shown in Figure 19. After the cavity vanishes, the downstream propagation must begin all over again. Regardless of the modeling approach, periodically occurring leading edge cavitation on the rudder and the propeller blades is observed. When utilizing LES, a cavitating hub vortex emerges, which interacts with the rudder's leading edge. This demonstrates that adaptive refinement of cavities inside the stationary part of the mesh and in interaction with solid obstacles is possible, which is one of the main objectives of this work. However, it should be noted that in future work, a numerical study of the E779A propeller should be carried out, which allows validation against an experimentally studied operating point and simulates the cavitating tip vortex in interaction with the rudder.

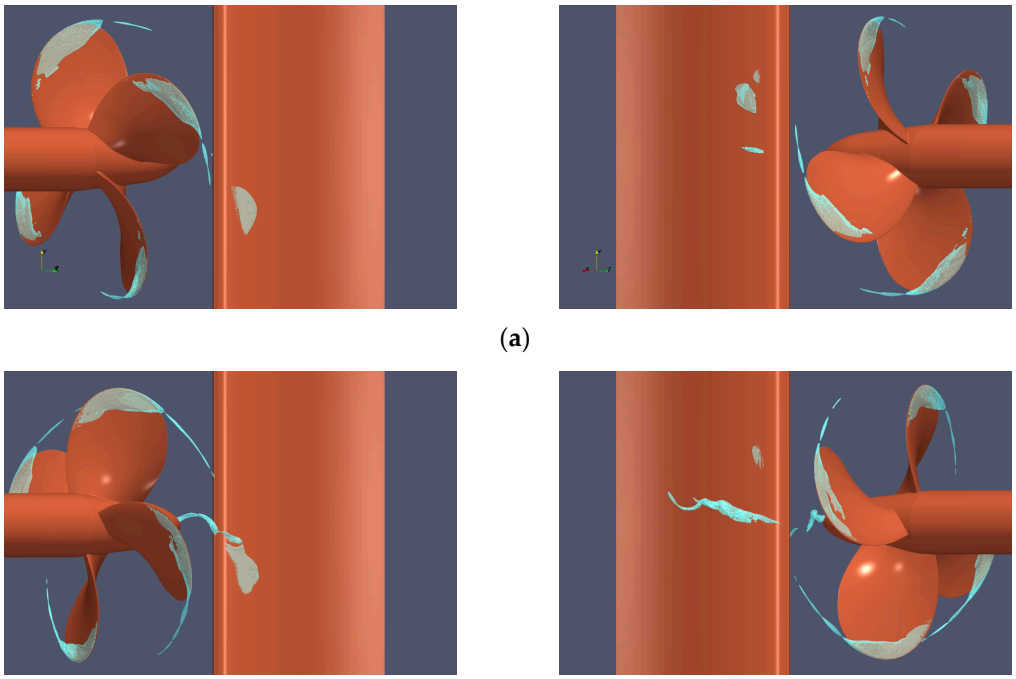

(**a**)

(**b**)

Figure 18. Comparison of cavitation $\alpha = 0.5$ isosurfaces, (**a**) RANS, (**b**) LES, E779A propeller with rudder.

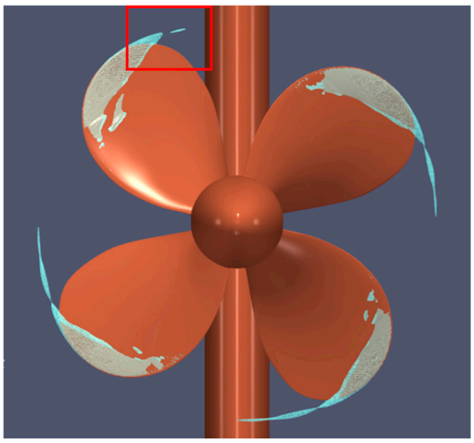

Figure 19. Periodical dissolving of the cavitating tip vortex after passing the twelve o'clock position marked in red, LES, E779A propeller with rudder.

4. Discussion

The goal of this study is to investigate to what extent AMR methods are applicable for sufficiently refining trailing vortices emerging from complex lifting geometries such as underwater propellers and, furthermore, interacting with rigid bodies in the surroundings. To ensure the practical application of the AMR method, it should be capable of adaptively refining transient computational setups with dynamic meshes and interface interpolation in combination with feasible computational effort. The key findings in this study are the following.

- When considering the computational effort, a significant increase in CPU time is evident, especially in cavitating conditions. Applying AMR at every time step for isolated propellers without inclination and uniform inflow is considered to be impractical since the adaptively refined cavitation area is not expected to change in an unpredictable way relative to the propeller. For this application, a single AMR step in combination with a longer rotating mesh region covering the whole axial range of interest should be sufficient and significantly less computationally demanding.
- Applying AMR at every time step is reasonable as a refinement setup in the presence of appendages such as a rudder, as otherwise, it is not possible to continuously resolve the cavities.
- The chosen adaptive refinement criterion for the trailing vortices in wetted conditions is the Q-criterion. In cavitating conditions, multi-criterion refinement is performed utilizing Q and the phase interface α. Under both conditions, sufficient refinement of the tip vortex region is achieved, successfully capturing the cavitation of the tip and hub vortex in the case of an isolated propeller with a satisfactory axial extent in the slipstream while exceeding the interface into the stationary part of the mesh. For the VP1304 propeller, this is in satisfactory accordance with the observed cavitation structure in the experiment and other vortex refinement techniques from the literature. Using the LES shows that the cavitating tip vortex is depicted significantly longer in the wake, which is advantageous if the objective is to investigate the interactions of trailing vortices with slipstream obstacles. However, the computational effort is significantly increased. RANS methods are usually sufficient to predict cavitation regions in the near wall region of the propulsor during the development of propulsion systems.
- Utilizing protected refinement regions allows constraining the AMR in areas of interest, namely the tip and hub vortex region. In the current implementation, it is not possible to declare protected regions inside the AMI, which, if a sufficiently fine refinement cell size is selected, leads to the refinement of secondary trailing vortices that may not be of interest and increase the cell count.
- For the propeller–rudder configuration, the observation of the refined mesh based on the Q-criterion and the cavitating hub vortex shows that an adequate refinement

outside the AMI near the rudder surface boundary is always possible if the initial mesh in the region of the protected boundary layer is sufficiently refined. This demonstrates that the adaptive refinement of cavities moving relative to the propeller in an unpredictable trajectory is possible.

- For the setups utilized, AMR is only applied prior to the calculation of the new time step. This leads to inaccuracies and instabilities in the flow prediction as parts of the relevant flow details are calculated on an unrefined mesh. When using a PIMPLE algorithm for solving, AMR steps at every outer corrector loop could overcome this issue; however, it would increase the CPU time even more.
- A major concern is instability, probably due to mapping issues between the generated grids, which creates unphysical fluxes and discontinuous gradients, enhanced in cavitating conditions, where unphysical pressure pulses occur at recently coarsened cells. This is highly undesirable since it prevents the numerical evaluation of underwater radiated noise, which is a fundamental purpose of this work. This issue, however, should be software-related, and the general use of AMR in combination with noise evaluation for the investigated purposes should be possible. In the authors' opinion, AMR, in general, is a promising tool for enhancing noise and cavitation erosion prediction capabilities in CFD due to its ability to resolve cavitating tip vortices in the presence and interaction of slipstream obstacles.

In the scope of this study, it is not possible to simulate the cavitating tip vortex interacting with the rudder and to validate the results with the experiment. This remains a task for future studies. Future studies with an inclined shaft and non-uniform inflow should be carried out in order to assess the influence on the load balance. Additional future work in improving dynamic load balancing is necessary, as it is not possible to use AMR in combination with arbitrary mesh interfaces for the CFD code used. Overall, minimizing processor imbalance when using AMR is important to address, as it can influence the computational costs significantly.

Assuming the above issues regarding stability and high computational costs are resolved in future work, AMR is a promising method for OpenFOAM distributions and other CFD codes for sufficiently refining the tip and hub vortices, in combination with transient propeller simulation, including a sliding mesh interface and the presence of rigid bodies in the surroundings.

Author Contributions: Conceptualization, J.K. and M.A.-M.; methodology, J.G. and J.K.; software, J.G.; investigation, J.G.; data curation, J.G.; writing—original draft preparation, J.G.; writing—review and editing, M.A.-M. and M.N.; supervision, M.A.-M. and M.N.; project administration, M.A.-M. and M.N.; funding acquisition, J.K. All authors have read and agreed to the published version of the manuscript.

Funding: This research was funded by BMWK, grant number 03SX560A, as Project "Red-Emi".

Institutional Review Board Statement: Not applicable.

Informed Consent Statement: Not applicable.

Data Availability Statement: Data are contained within the article.

Acknowledgments: The authors are very grateful for the support from Engys Ltd. during the trial of the AMR functionality and for providing the code.

Conflicts of Interest: Author J.G. and author J.K. was employed by the company SCHOTTEL GmbH. The remaining authors declare that the research was conducted in the absence of any commercial or financial relationships that could be construed as a potential conflict of interest. The funders had no role in the design of the study, in the collection, analyses, or interpretation of data, in the writing of the manuscript, or in the decision to publish the results.

References

1. Bretschneider, H.; Bosschers, J.; Choi, G.H.; Ciappi, E.; Farabee, T.; Kawakita, C.; Tang, D. Specialist Committee on Hydrodynamic Noise. In Proceedings of the Final Report and Recommendations to the 27th ITTC, Copenhagen, Denmark, 31 August–5 September 2014.
2. Van Terwisga, T.; Fitzsimmons, P.; Ziru, L.; Foeth, E. Cavitation Erosion—A review of physical mechanisms and erosion risk models. In Proceedings of the 7th International Symposium on Cavitation, Ann Arbor, MI, USA, 17–22 August 2009.
3. Frisk, G. Noiseonomics: The relationship between ambient noise levels in the sea and global economic trends. *Sci. Rep.* **2012**, *2*, 437. [CrossRef] [PubMed]
4. Williams, R.; Wright, A.J.; Ashe, E.; Blight, L.K.; Bruintjes, R.; Canessa, R.; Clark, C.W.; Cullis-Suzuki, S.; Dakin, D.T.; Erbe, C.; et al. Impacts of anthropogenic noise on marine life: Publication patterns, new discoveries, and future directions in research and management. *Ocean Coast. Manag.* **2015**, *115*, 17–24. [CrossRef]
5. Veritas, D.N. Silent Class Notation. In *Rules for classification of ships-Newbuildings*; DNV: Bærum, Norway, 2010.
6. Viitanen, V.; Siikonen, T.; Sanchez-Caja, A. Numerical Viscous Flow Simulations of Cavitating Propeller Flows at Different Reynolds Numbers. In Proceedings of the Sixth International Symposium on Marine Propulsors, Rome, Italy, 26–30 May 2019.
7. Asnaghi, A.; Svennberg, U.; Bensow, R.E. Large Eddy Simulations of cavitating tip vortex flows. *Ocean Eng.* **2020**, *195*, 106703. [CrossRef]
8. Windt, J.; Bosschers, J. Influence of local and adaptive mesh refinement on the tip vortex characteristics of a wing and a propeller. In Proceedings of the VI International Conference on Computational Methods in Marine Engineering, Rome, Italy, 15–17 June 2015.
9. Lloyd, T.; Vaz, G.; Pijpkema, D.; Reverberi, A. Computational fluid dynamics prediction of marine propeller cavitation including solution verification. In Proceedings of the Fifth International Symposium on Marine Propulsors, Espoo, Finland, 12–15 June 2017.
10. Yvin, C.; Muller, P. Tip Vortex Cavitation Inception Without a Cavitation Model. In Proceedings of the 19th Numerical Towing Tank Symposium, St Pierre d'Olerion, France, 3–4 October 2016.
11. Sezen, S.; Atlar, M. An alternative Vorticity based Adaptive Mesh Refinement (V-AMR) technique for tip vortex cavitation modelling of propellers using CFD methods. *Ship Technol. Res.* **2021**, *69*, 1–21. [CrossRef]
12. Krasilnikov, V. CFD modelling of hydroacoustic performance of marine propellers: Predicting propeller cavitation. In Proceedings of the 22nd Numerical Towing Tank Symposium, Tomar, Portugal, 29 September–1 October 2019.
13. Kimmerl, J.; Mertes, P.; Abdel-Maksoud, M. Application of Large Eddy Simulation to Predict Underwater Noise of Marine Propulsors. Part 1: Cavitation Dynamics. *J. Mar. Sci. Eng.* **2021**, *9*, 792. [CrossRef]
14. Kimmerl, J.; Mertes, P.; Abdel-Maksoud, M. Application of Large Eddy Simulation to Predict Underwater Noise of Marine Propulsors. Part 2: Noise Generation. *J. Mar. Sci. Eng.* **2021**, *9*, 778. [CrossRef]
15. Kimmerl, J.; Abdel-Maksoud, M.; Nataletti, M.; Savio, L. Acoustic Comparison of a Ship-Propeller Model in Cavitating Conditions with LES and FWH-Method. In Proceedings of the 7th International Symposium in Marine Propulsors, Wuxi, China, 17–21 October 2022.
16. Yilmaz, N.; Atlar, M.; Khorasanchi, M. An improved Mesh Adaption and Refinement approach to Cavitation Simulation (MARCS) of propellers. *Ocean Eng.* **2019**, *171*, 139–150. [CrossRef]
17. Yilmaz, N.; Atlar, M.; Fitzsimmons, P.A. An Improved Tip Vortex Cavitation Model for Propeller-Rudder Interaction. In Proceedings of the 10th International Cavitation Symposium, Baltimore, MD, USA, 14–16 May 2018.
18. Yilmaz, N.; Aktas, B.; Sezen, S.; Atlar, M.; Fitzsimmons, P.A.; Felli, M. Numerical Investigations of Propeller-Rudder-Hull Interaction in the Presence of Tip Vortex Cavitation. In Proceedings of the 6th International Symposium in Marine Propulsors, Rome, Italy, 26–30 May 2022.
19. Menter, F.; Ferreira, J.C.; Esch, T.; Konno, B. The SST Turbulence Model with Improved Wall Treatment for Heat Transfer Predictions in Gas Turbines. In Proceedings of the International Gas Turbine Congress, Tokyo, Japan, 2–7 November 2003.
20. Ferziger, J.H.; Peric, M. *Computational Methods in Fluid Dynamics*, 2nd ed.; Springer Berlin: Berlin/Heidelberg, Germany, 2002. [CrossRef]
21. Schmitt, F. About Boussinesq's turbulent hypothesis: Historical remarks and a direct evaluation of its validity. *Comptes Rendus Mécanique* **2007**, *335*, 617–627. [CrossRef]
22. ENGYS, Ltd. HELYXcore Source Code, Version 3.5.0; File: Smagorinsky.C, [Source Code]. 2022. Available online: https://github.com/OpenFOAM/OpenFOAM-6/blob/master/src/TurbulenceModels/turbulenceModels/LES/Smagorinsky/Smagorinsky.C (accessed on 10 September 2023).
23. Hunt, J.; Wray, A.; Moin, P. Eddies, streams, and convergence zones in turbulent flows. In *Studying Turbulence Using Numerical Simulation Databases—II Proceedings of the 1988 Summer Program*; Stanford University: Stanford, CA, USA, 1988.
24. ENGYS, Ltd. HELYXcore Source Code, Version 3.5.0; File: SchnerrSauer.C, [Source Code]. 2022. Available online: https://www.openfoam.com/documentation/guides/latest/api/SchnerrSauer_8C_source.html (accessed on 10 September 2023).
25. Schnerr, G.; Sauer, J. Physical and Numerical Modelling of Unsteady Cavitation Dynamics. In Proceedings of the 4th International Conference on Multiphase Flow, New Orleans, LA, USA, 27 May–1 June 2001.
26. Schnerr, G.; Sauer, J. Unsteady Cavitating Flow—A New Cavitation Model Based on a Modified Front Capturing Method and Bubble Dynamics. In Proceedings of the FEDSM'00, Boston, MA, USA, 11–15 June 2000.

27. Kimmerl, J.; Mertes, P.; Abdel-Maksoud, M. Turbulence Modelling Capabilities of ILES for Propeller Induced URN Prediction. In Proceedings of the SNAME Maritime Convention 2020, Houston, TX, USA, 29 September–2 October 2020.
28. ANSYS, Inc. Adapting the Mesh. In *ANSYS-FLUENT-Theory Guide, 12.0*; ANSYS, Inc.: Canonsburg, PA, USA, 2009; pp. 19–28.
29. Rettenmaier, D.; Deising, D.; Ouedraogo, Y.; Gjonaj, E.; De Gersem, H.; Bothe, D.; Tropea, C.; Marschall, H. Load balanced 2D and 3D adaptive mesh refinement in OpenFOAM. *SoftwareX* **2019**, *10*, 100317. [CrossRef]
30. Barkmann, U.; Heinke, H.; Lübke, L. Potsdam Propeller Test Case Description. In Proceedings of the Second International Symposium on Marine Propulsors, Hamburg, Germany, 15–17 June 2011.
31. Heinke, H. *Cavitation Tests with the Model Propeller VP1304, Report 3753*; Schiffbau-Versuchsanstalt Potsdam GmbH: Potsdam, Germany, 2011.
32. Salvatore, F.; Pereira, F.; Felli, M.; Calcagni, D.; Felice, F. *Description of the INSEAN E779A Propeller Experimental Dataset*; Institute of Marine Engineering CNR-INM: Singapore, 2006.
33. Liu, F. A Thorough Description Of How Wall Functions Are Implemented In OpenFOAM. In *Proceedings of CFD with OpenSource Software*; Nilsson, H., Ed.; Chalmers University of Technology: Gothenburg, Sweden, 2016.
34. Kuiper, G. Cavitation Inception on Ship Propeller Models. Ph.D. Thesis, TU Delft, Wageningen, The Netherlands, 1981.